Comparisons of VHF Meteor Radar Observations in the Middle Atmosphere With Multiple Independent Remote Sensing Techniques.

Daniel L. McIntosh, BSc. (Hons)

Thesis
submitted for the degree of
DOCTOR OF PHILOSOPHY
at the
UNIVERSITY OF ADELAIDE
School of Chemistry and Physics
Discipline of Physics

August 2009

Chapter 1

Introduction

The need to obtain profiles of atmospheric parameters in the Mesospheric and Lower Thermospheric (MLT) region has increased, especially in the last decade. The driving force behind this is the need for a better understanding of the aeronomy and dynamics of the MLT region and its role in determining the evolution of Earth's climate. Due to the high altitude of the MLT region and the technology available, observations of atmospheric parameters such as winds and temperature have always proved to be a challenge for scientists trying to develop a better understanding of its dynamics and the role it plays. The significant costs associated with rocket observations, plus their inability to obtain more than a brief "snapshot" of the atmosphere, has served to promote the development of technologies such as ground-based radars along with ground and space-based optical techniques for monitoring the MLT region.

Every technique used in the observation of the atmosphere and the MLT region in particular has its respective strengths and weaknesses. When these techniques are combined, each of them serves to complement the other as well as supplementing the other's short comings. In order to do so, an understanding of how each of these techniques compares is critical. We also seek to improve these techniques. Part of the focus of this study has been in the development and refinement of a high-powered meteor radar at Buckland Park, Australia, to investigate the performance of using high power in meteor observations. Meteor radar observations have been in existence since the early to mid 20th century [Nagaoka, 1929, Skellett, 1931]. Techniques used in radar observations of meteors have included Continuous-Wave (CW) forward scatter (bi-static) [Cevolani et al., 1998], directed narrow beam observations

[Cervera and Reid, 1995, Singer et al., 2008] and all-sky interferometric observations [Jones et al., 1998, Holdsworth et al., 2004]. The focus of this study is on using the all-sky interferometirc technique. The meteor technique has experienced a resurgence in popularity due to its ability to obtain temperature estimates as well as wind profiles in the MLT region. Despite its long history in atmospheric science, meteor radar techniques are continually developing and still require investigation into the quality of results produced. Take for example the measurement of MLT winds by radar techniques. Both meteor and Medium Frequency (MF) radars employ coherent scatter techniques on different scattering mechanisms. Each scattering mechanism is dependent upon different physical processes as discussed in Chapter 2. For radar observations in the MLT region, there are three mechanisms for the return of radio waves in the MLT region; these include Turbulent (Bragg) Scatter, Thermal (Thompson) Scatter and Fresnel Reflection or Fresnel Scatter. The three scattering mechanisms can be characterized as follows:

- Thermal Scatter - Scatter results from the scattering of a small part of the incident radio wave by variations in the refractive index that are caused by random motion in the electron density due to thermal motion of ions and electrons.

- Turbulent Scatter - Scatter results from the scattering of radio waves from irregularities that are produced by turbulence, with irregularity scales being on the order of half the radar wavelength (λ).

- Fresnel Scatter - Scatter results from irregularities in the radio refractive index transverse to the radio wave propagation direction that are thin compared with λ. In the case of vertical incidence, the horizontal extent of the irregularity must be greater than one Fresnel zone ($(z\lambda)^{1/2}$), where z is the height of the scatterer. In practice, the horizontal extent of the irregularity need only be larger than the width of the radar beam. The vertical variation in refractive index need only be less than $\lambda/4$ to produce strong enough returns.

For further information on scattering mechanisms in the MLT region, the reader is directed to Gage and Balsley [1980] and Reid [1990].

In the case of the meteor technique, the radar uses meteor trails typically with a diameter $\sim \lambda/2$ as a back scattering target; the number of trails varies during the course of the day. In the case of the MF radar, scattering is primarily due to Fresnel and Bragg scatter, with Fresnel scatter being dominant in the case of back scatter. The electron density in the MLT region is influenced by solar radiation and as such there is a depletion of scatterers at night due to ion-electron recombination. Since the number of scatterers varies for each technique through the course of the day, a better understanding of both the statistical accuracy of these techniques as well as variability of the statistical accuracy is required. The understanding of statistical accuracy is not limited to just meteor and MF wind comparisons. What happens in the case of comparing winds from two co-located meteor radars operating at different frequencies? Does an increase in the number of detectable echoes improve statistical reliability of wind estimates? These questions are addressed within this study along with ascertaining how well different techniques agree. Furthermore we seek to extend this to the comparison of temperatures derived using meteor observations and answer the question of how well do these observations agree with other accepted techniques.

In this chapter we seek to paint a picture of the environment we are attempting to characterize. We begin by providing some perspective to the reader of the structure of the atmosphere, the location of the MLT region and where meteor observations occur. Also described are some of the physical processes that occur within this region. We subsequently provide some information on the three locations in which radar and optical data were obtained for this study. Finally we provide the scope of this thesis which outlines its structure and provides the reader with a map that we follow in our journey to better understand the meteor technique and its role in atmospheric research.

1.1 Structure of the Atmosphere

The vertical structure of the atmosphere can be classified according to the different physical properties that are observed as a function of height. The most common means of classifying the structure of the atmosphere is the variation of atmospheric temperature as can be seen in Figure 1.1. The vertical structure varies with geographical location and season, however the basic overall structure is similar between geographical location and season. This can be observed in the turning points of the temperature profile between

the three locations in Figure 1.1. The regions in ascending height are denoted the "troposphere", "stratosphere", "mesosphere" and "thermosphere". The transition regions between each of these regions where local extrema occur are labeled "tropopause", "stratopause", and "mesopause" respectively. The behavior of the temperature profile in Figure 1.1 can be understood by the dominant processes that occur at specific heights.

Unlike the temperature structure of the lower atmosphere, the observed temperature structure in the mesosphere, that is colder in summer than in winter, can be attributed to small-scale gravity waves interacting with zonal circulation [Mayr et al., 2009]. The gravity waves propagate up through the stratosphere where they interact with the zonal circulation as can be seen in the study by Mayr et al. [1997]. Eastward propagating gravity waves interact and deposit energy and momentum into the eastward winds of the winter hemisphere, while those that propagate westward interact with the zonal winds in summer. The wave filtering and resulting momentum deficits that accompany this process result in the gravity waves generating reversing zonal winds in the upper mesosphere. This results in an increase, through the Coriolis force, in the magnitude of the meridional circulation (summer to winter) to such an extent that it dominates the energy budget of the region. The dynamical cooling associated with this process removes more energy from the summer hemisphere than what is deposited by solar radiation. As a result, the temperatures in the mesopause region are cooler in summer than in winter. The very large vertical winds at high latitudes that result from the global-scale meridional circulation across the equator diverge and converge at the poles in summer and winter respectively. The resulting effect of these winds produce, through the result of adiabatic cooling and heating, the large temperature variations that can be observed in the temperature profiles for Davis depicted in Figure 1.1.

AURA MLS temperature data was used in this study for comparison with temperatures derived using the meteor technique at Davis Station, Buckland Park (BP) and Darwin. The data are also concurrent with the meteor data, making it ideal for the comparisons undertaken in this study. The AURA instrument also provides a long term data set that can be used in long term climatalogy studies. The mesosphere is sensitive to changes in climate and as such the AURA data also provides a means of studying climate change through long term observations of the mesospheric region. The temperature profiles in Figure 1.1 represent summer (December to February) and winter

(June to August) seasonal averages derived from 2004 to 2008 AURA MLS satellite data. For each day there are two passes of the satellite separated by approximately 12 hrs. The AURA MLS data was Version 2.2, which is not recommended for scientific use for pressure levels less than approximately 0.001 hPa (0.1 Pa). This pressure level corresponds to a geometric height of approximately 92 km, which is the approximate top of the MLS limb scan. Data above this level comes from either a climatological a priori or an extrapolation by the smoothing operator of the retrieved layers below. For further details on the usage of AURA MLS data, the reader is referred to the data usage section of the AURA MLS homepage[1] and the temperature evaluation paper by Schwartz et al. [2008]. Both documents recommend limiting the data to pressure levels between 316 hPa (3.16×10^4 Pa) and 0.001 hPa (0.1 Pa). The vertical region bounded by the thick purple lines in Figure 1.1 indicate the height region where the majority of meteor echoes are detected at VHF frequencies.

[1] http://mls.jpl.nasa.gov/data/

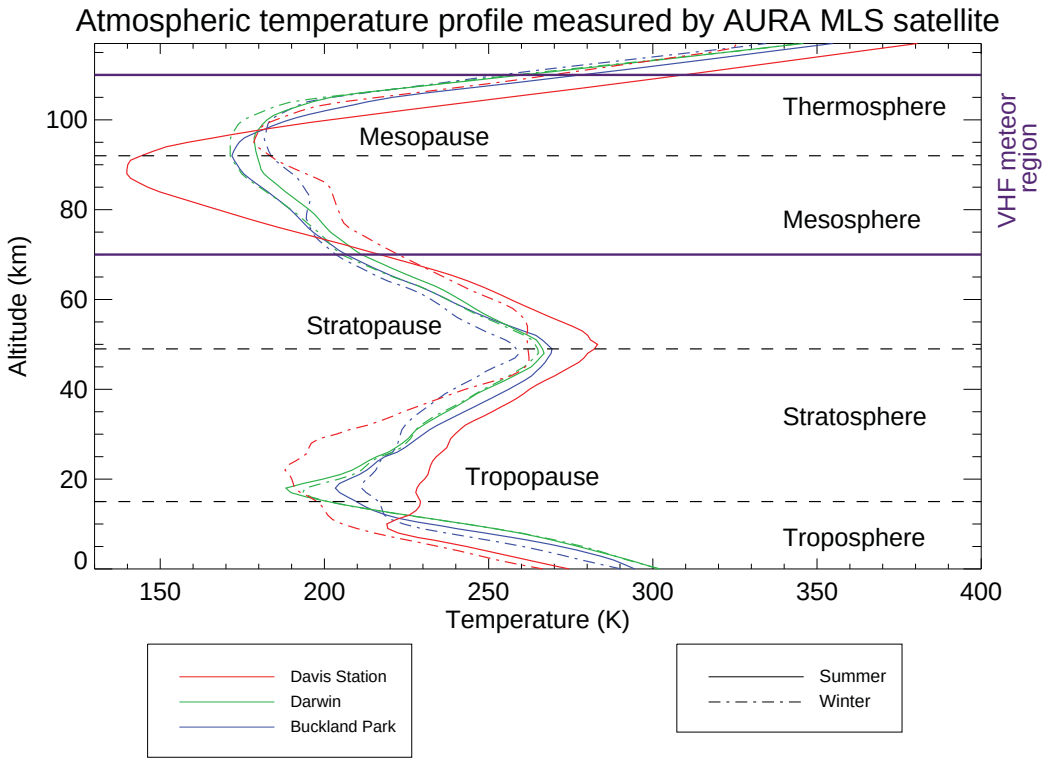

Figure 1.1: Atmospheric temperature profiles at Davis Station, Antarctica, Buckland Park, South Australia, and Darwin, Northern Territory. The temperature profiles represent summer (December to February) and winter (June to August) seasonal averages derived from 2004 to 2008 AURA MLS satellite data. For each day there are two passes of the satellite separated by approximately 12 hrs. Version 2.2 of the AURA MLS data was used in the generation of these profiles and temperature comparisons in Chapter 8.

1.1.1 The Ionosphere

The ionosphere is the region of the atmosphere (altitudes greater than approximately 60 km) containing a high enough concentration of electrons to effect the propagation of radiowave signals. This high concentration of electrons is produced along with positive ions due to the ionization of molecular oxygen, nitrogen and nitrogen monoxide by incident short-wave solar radiation and cosmic rays. The electron concentration can be described by a complex series of equations which vary as a function of height, season and time of day. The form and origin of these equations is beyond the scope of this study and as such not presented. See Rishbeth and Garriot [1969] for a more detailed description.

If we take into account the Earth's geomagnetic field, the ionosphere can be observed to act as a doubly refracting medium [Davies, 1990]. The two modes of propagation for radio waves in this region are denoted the "ordinary" (O) mode and the "extraordinary" (X) mode. Both modes are polarized in opposite senses with respect to the other and propagate with differing group velocities. These two modes of propagation play an important role in atmospheric observations with MF radar in the mesospheric and lower thermospheric region. The difference in the refractive indices experienced by both O and X mode polarization accounts for the difference in the absorption height and hence vertical coverage of the radar. O-mode is used for day time observations as it does not suffer the same level of absorption experienced by X-mode polarization during the day. X-mode is used for night time observations where it does not suffer the same level of absorption experienced during the day. Later on in this thesis we consider the effects of utilizing both modes in the observation of winds in the MLT region, along with the quality of wind estimates each mode is capable of offering with MF radar observations.

The Very High Frequency (VHF) band is defined between 30 MHz and 300 MHz. In this study we make use of VHF radars operating at 33.2 MHz and 55 MHz. For VHF less than 50 MHz, the main effect of the ionosphere on radio wave propagation is Faraday rotation, angular refraction and time delay. The main effect of the ionosphere for most of the VHF band is to scatter radio energy by irregularities. For a more comprehensive description of propagation of radio waves in the ionosphere and of radio waves in the VHF and other frequency bands, the reader is directed to Davies [1990].

The individual regions of the ionosphere are described according to the peaks in electron concentration by (in ascending height) the D, E, F_1 and F_2 regions. The D-region lies between approximately 60 and 90 km, which roughly corresponds to the mesosphere as defined in Figure 1.1, and is the focus of this study. The D-region is formed primarily by the ionization of nitrous oxide by the Lyman-α Hydrogen emission line. To a lesser extent ionization of molecular oxygen by the Lyman-β Hydrogen emission line and ultra-violet radiation also contributes to the D-region formation. The D-region provides for "partial-reflection" of radar signals at MF and VHF due to small discontinuities in the refractive index of the atmosphere, which is discussed further in Chapter 2 . The E-region typically peaks at 110 km.

1.2 Observation Sites

Ground based observations of mesospheric parameters were conducted at three sites with a variety of equipment to obtain measurements and comparisons. These sites were Buckland Park, Darwin and Davis Station, Antarctica, as shown in Figure 1.2.

1.2.1 Buckland Park Field Site

The Buckland Park field site is located approximately 35 km north of Adelaide, South Australia (34.5°S, 138.5°E). A number of instruments for observation of atmospheric parameters are established there. These include a Medium Frequency (MF) spaced antenna and Doppler radar, three-field photometer, spectrometer, automatic weather station and a Very High Frequency (VHF) Doppler Stratospheric Tropospheric (ST) meteor radar hybrid. The evolution of the meteor radar and its present configuration is presented in detail in Chapters 3, 4 and 5. The co-location of multiple instruments for comparison of winds and temperature in the Mesospheric and Lower Thermosphere (MLT) region is one the driving forces behind this study. The results of the instruments from BP can be found on the Atmospheric Physics Group's web page[2].

[2]http://www.physics.adelaide.edu.au/atmospheric/

1.2.2 Davis Station

Davis Station (68.5°S, 78°E) is located approximately 4600 km south-south-east of Perth, Western Australia, on the Antarctic continent. A number of instruments for observation of atmospheric parameters are established there. These include a MF radar, 33.2 MHz VHF meteor radar, 55 MHz spaced antenna and Doppler ST/meteor hybrid radar, lidar, spectrometer, Fabry-Perot interferometer and Ionosonde. The 33.2 MHz meteor radar is similar to the Darwin meteor system and the 55 MHz ST/meteor hybrid system is similar to the BP system except the Davis ST uses spaced antenna techniques. Descriptions of the meteor radars can be found in Chapter 3 and results for instruments can be found on the Australian Antarctic Division's web page[3].

1.2.3 Darwin

The Darwin 33.2 MHz meteor radar is located at the Australian Government Bureau of Metorology ARM site which is approximately 14 km east-north-east of Darwin, Northern Territory (12.5°S, 130.5°E). The site is used primarily by the Bureau for monitoring the troposphere, however the Atmospheric Physics Group was given access to the site to establish the meteor radar system as a part of the Tropical Warm Pool-International Cloud Experiment (TWP-ICE) campaign during 2004-2005 [May and Mather, 2005]. The purpose of the campaign was to investigate gravity wave coupling between the lower and middle atmosphere which results from tropical cloud formations. The Darwin meteor radar is discussed in detail in Chapter 3.

[3]http://www.aad.gov.au/davis/

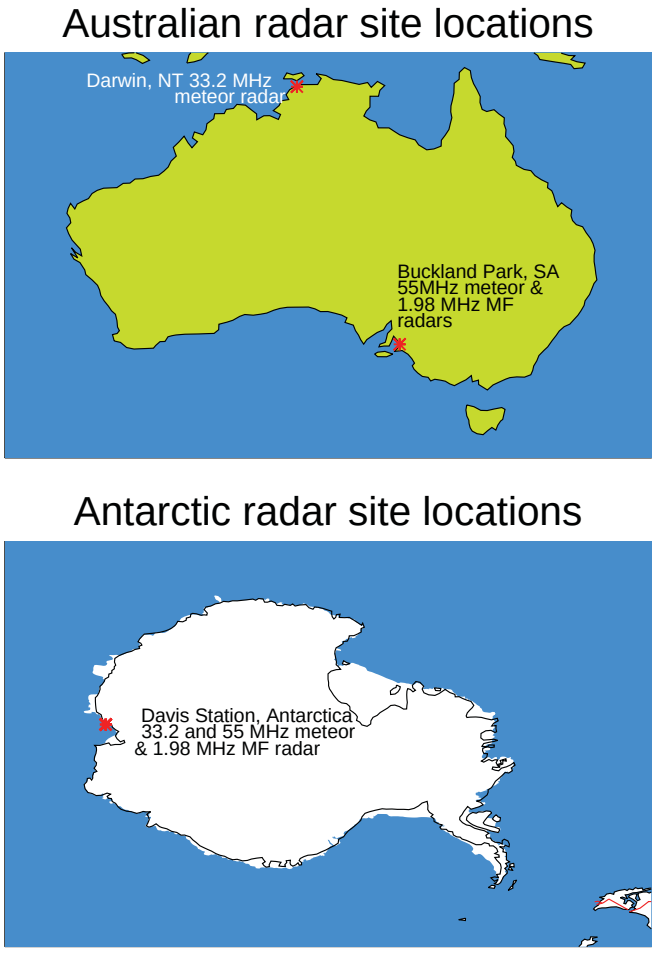

Figure 1.2: The maps above show the locations of the radars used within Australia and in the Australian Antarctic Territory.

1.3 Scope of Thesis

During the course of the research described in this thesis, a hybrid VHF ST/meteor radar system was developed based upon an existing VHF ST radar system and operated over a three year period and continues to operate today. Over this period the system has been steadily refined and experimented with and has achieved all the initial design goals despite setbacks due to involuntary damage to radar components.

Chapter 3 describes the reasons behind the configuration and chosen type of the meteor radar used. This chapter details the transmission, reception and acquisition of meteor radar signals as performed by the numerous radars used in this study. A description of the principles of functionality of the acquisition system are also applicable to the MF radar systems used. Chapter 3 also describes the evolution of the high-powered transmit antenna from using a single Valve Transmitter (VTX) Pre-Amplifier (PA) to using six along with the development of the required 1:2 splitter-combiner. Chapter 4 describes in detail the design process, equations and *EZNEC* numerical modeling used to develop the high-powered transmit antenna that was later fabricated and installed at BP by Broadband Propagation Pty Ltd. Also presented are the steps required for fabrication and assembly of the antenna. Chapter 5 describes in detail the design and performance of the high-powered 1:2 splitter combiner that is used with the meteor system. The six outputs from the VTX were combined into a single output via a 6:1 combiner which was then required to be split to feed both arms of the high-powered transmit antenna. Also described is the replacement 1:2 splitter-combiner which is used with the new STX-II transmitter in operation at the Buckland Park field site as a part of routine ST operations. This is because the STX-II transmitter has two outputs which can feed the meteor antenna directly.

In Chapter 6 the echo rate performance of meteor radars is discussed with the verification of the echo rate as a function of radar parameters as published by McKinley [1961] using different transmitters with the high-powered transmit antenna. Also discussed is the verification of radar output power along with its correspondence to the settings made within the radar configuration software. A procedure for receiver gain calibration is also discussed along with its use in determining both received echo power from a typical underdense meteor trail along with the trail line charge density.

Chapter 7 details and discusses the comparison of mesospheric wind es-

timates made by co-located independent radar systems using the statistical comparison technique outlined in this chapter and in Hocking et al. [2001] at Davis Station and BP. Davis Station permits a unique comparison in that it has three co-located independent systems; two of which utilise the same technique for generating wind estimates. A comparison of this type has never been performed before and serves to provide a unique insight into the meteor and MF techniques. In general, the results of the statistical comparison technique used require a priori knowledge of the uncertainty associated with one set of measurements in order to determine a unique solution for the relationship between two independent sets of measurements of the same quantity. The three radar systems at Davis Station measuring mesospheric winds (two meteor and one MF) allows for this to occur. This is discussed in detail in Chapter 7 along with the results of comparing the independent sources of mesospheric wind estimates.

Chapter 8 details and discusses mesospheric temperature estimates derived from meteor radar diffusion coefficient estimates and compares the results to satellite temperature estimates at all three locations and to temperature estimates derived from OH air glow emissions at Davis Station and BP. A thesis summary with suggestions for future research is provided in Chapter 9.

Chapter 2

Observation Techniques

While the main focus of the study is on meteor radar observations of MLT winds and temperatures, other sources of data have been used for comparison against the measurements made by meteor radars at Davis Station, Buckland Park (BP) and Darwin. In this chapter we discuss the principles behind each of the techniques as well as provide brief descriptions of the instrumentation. The meteor and MF radar instrumentation are discussed in detail in the following chapters. We begin with a brief overview of meteor radar, followed by descriptions of the techniques involved. We subsequently discuss the MF radar, satellite, falling sphere and airglow techniques.

2.1 Meteor Radar: Overview

Radar observations of the MLT region have been in effect since the early decades of the 20^{th} century. Appleton and Barnett (1925, England) and Breit and Tuve (1926, USA) were credited with the examination of radio waves reflected from thin layers in the 70 to 120 km region of the atmosphere [McKinley, 1961]. In the period 1929-1930 it was observed by radio physicists that there were a significant number of ionospheric returns from the E-region ($\sim$100 km). While the formation of the ionospheric scatterers during the day could be attributed to solar radiation, this could not explain the returns being observed during the night time period. The first person to suggest that the night time returns are the result of meteors was Nagaoka (1929, Japan). Nagaoka hypothesised that meteor trails served to absorb electrons thus decreasing the electron density of the atmosphere in the local region of

the meteor trail. This would result in a gradient in the radio refractive index of the atmosphere in the localised tail region. It wasn't until 1935 where Skellet was credited with the realisation that meteors in fact contributed to the electron density of the atmosphere in the local region of the tail. The resulting effect is electron density gradients in the meteor region (70 - 120 km for the majority of echoes) to which coherent scatter techniques could be applied. Observations of meteors with radar was not introduced in Australia until 1952 with the work of Robertson, Libby and Elford at the University of Adelaide [Elford and Robertson, 1953, McKinley, 1961, Roper, 2008].

Meteor radar systems have developed over the years with system configurations including, Continuous-Wave (CW) forward scatter (bi-static) [Cevolani et al., 1998], directed narrow beam [Cervera and Reid, 1995, Singer et al., 2008], and all-sky interferometric systems [Jones et al., 1998, Holdsworth et al., 2004]. The research described in this thesis continues the development of interferometric type systems, however the fundamental principles in which they operate upon have remained the same. Meteor radar observations entail the use of coherent scatter techniques for the detection of meteor trails. Meteor trail interaction with radio waves exhibit certain characteristics which enable the determination of atmospheric parameters such as wind velocity, atmospheric temperature and pressure. Until the work of Jones et al. [1998], meteor radar systems employed antenna arrays with antenna spacings $\leq 0.5\lambda$. This mode of operation has been shown to introduce errors in Angle of Arrival (AOA) estimates as discussed in Section 2.3. The radars used during the course of this study were all interferometric meteor radars which employ the use of an interferometer for the detection of meteor echoes. A full description of the radar systems can be found in Chapter 3.

Meteor trails are sporadic in nature, the number of which varies throughout the course of the day. The variation in meteor echo events through the course of a days observation has been subject of study for some time [Cervera et al., 2004, Cervera and Elford, 2004]. This variation of the number of echoes in a particular window of time in a day can be attributed to the Earth's rotation and precession through space around the sun. If we take a single point of latitude and longitude on the Earth, then in the local morning hours, that point is moving towards the stream of meteors which has the effect of the Earth scooping up space debris which supplements the normal meteor activity. In the local evening hours, this point will in effect be moving away from the stream of meteors which leads to the observed decrease in meteor

detections during the local evening hours. See Figure 2.1. As we can see from the variation in the number of echoes (scattering targets) throughout the course of the day, this will obviously vary the statistical reliability of the technique. This variation in available scattering targets is discussed later on in this thesis when comparing data from the meteor technique with that of other techniques.

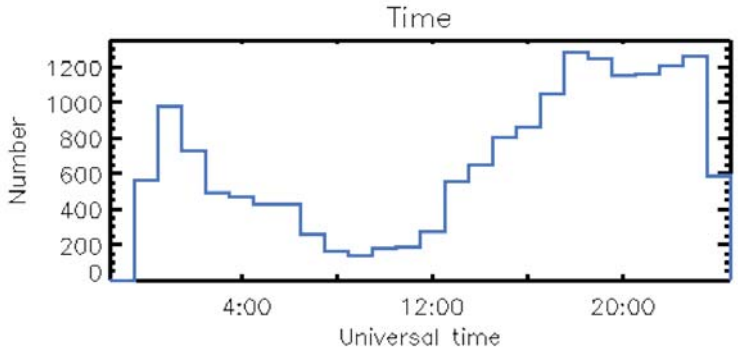

Figure 2.1: From this plot we can observe the variation in echo detections at Darwin throughout the course of the day. Note the horizontal axis is in universal time coordinates (UTC). Notice that the number of echoes maximizes at 20:00 UTC (5:30 Australian central standard time (CST)) and minimizes at 8:00 UT (17:30 CST). The number of meteors detected is over the entire height range distribution on the 17/12/2004.

2.2 Meteoric Diffusion Process

Meteors are classified as bodies which burn up upon entry into the Earth's atmosphere. A meteorite is the term given to a body which survives the entry process and impacts with the Earth's surface. As a meteor enters the Earth's atmosphere it undergoes an ablation process whereby the body breaks up due to friction between the body and the atmosphere. What is left in the wake of the meteor is a highly ionised trail along the trajectory of the meteor. The trail subsequently diffuses and drifts in the atmosphere. These physical processes are the fundamental basis of the meteor radar observations used in the derivation of mesospheric winds and temperatures in this thesis. Using

meteor radar, meteor echoes are classified as either undersense or overdense. A typical underdense meteor echo is classified as follows:

- The number of charged ions per unit metre (line charge density) of the trail is $\lesssim 10^{14}$ C.m^{-1}.
- The trail is instantaneously formed over the entire field of view of the radar.
- A radio wave is able to freely penetrate the trail.
- The trail diameter is $\leqslant \lambda/2$. (λ is the radar wavelength)
- Each individual electron behaves as if no other is present, such that secondary radiative and absorptive effects can be neglected (This is fundamental to the definition of an underdense trail).
- The life time of the trail is only a few seconds.

One of the main properties used in the classification of meteor trails is the line charge density. The line charge density is a measure of the number of charges contained within the trail volume along the axis of the trail in a unit length (1m). An underlying assumption is that the line charge density is constant along the trail axis at the point where the radar signal intersects and is scattered from the trail. Overdense echoes are considered to have electron line densities greater than 10^{14} C.m^{-1} and as such their echo characteristics are similar to that of a hard target as incident radio waves are unable to penetrate the trail as easily and their life time can exceed several minutes. Overdense echoes are rejected by the radar system as their echo characteristics can not be used by the system to estimate the diffusion rate of the trail and hence are outside the scope of this study. We have used the term 'freely penetrate' to describe the interaction between the meteor trail and the electromagnetic wave as one of the classifications of underdense echoes. Another means of trail classification is in terms of the trail's plasma frequency. Consider a small-volume plasma (e.g. meteor trail). The meteor trail can only exhibit overdense-like scattering behavior provided that the local plasma frequency is well above the frequency of the incident wave[Matthews, 2004]. Conversely, the meteor trail can only exhibit underdense-like characteristics provided the local plasma frequency is below frequency of the incident wave. The reader is directed to the work of Ratcliffe [1962], which investigates

and describes the process of reflection from plasmas as a function of wave vs plasma frequency and Matthews [2004] for a more comprehensive discussion on the role plasma and incident wave frequencies in the classification of classical meteor echo trails.

While it is accepted that atmospheric temperature and pressure serve to dictate diffusion rates of meteor trails, it has been shown by Younger et al. [2008] that atmospheric dust particles which are the remnants of past meteor trail events as well as ice crystal formation can influence diffusion rates of meteor trails depending upon the trail's line charge density. This fact along with the influence of geophysical phenomena on average estimates of meteor diffusion coefficients as suggested by Holdsworth et al. [2006] have been taken into account when using meteor diffusion coefficients to estimate mesospheric temperatures later in this thesis. We next discuss how the diffusion coefficient for a particular meteor trail can be estimated.

2.2.1 Meteor Diffusion Coefficient Estimates

The derivation of echo decay time and thus diffusion coefficient along with the diffusion process itself has been documented on several occasions (e.g. McKinley [1961], Jones and Jones [1990], Jones [1991, 1995]). While McKinley [1961] showed that an analytical solution is possible when a Gaussian distribution is assumed for the initial distribution of charge about the trail axis, Jones [1995] showed using a non-Gaussian initial distribution that the Fourier transform of the density distribution of the trail decays exponentially. McKinley [1961] first considers the case of no diffusion and shows from Fresnel diffraction theory that the received echo power P_r can be written as

$$P_r = 2.5 \times 10^{-32} P_t G_t G_r q^2 \left(\frac{\lambda}{R_0}\right)^3 \frac{C^2 + S^2}{2}, \tag{2.1}$$

where P_t is the transmitted power, G_t and G_r are the gain of the transmit and receive antennas, q is the line charge density of the trail, λ is the radar wavelength, R_0 is the perpendicular distance to the trail and C and S are the Fresnel integrals from diffraction theory. Using a Gaussian initial distribution, it can be shown that the total echo power from a thin slice of the trail of width ds is given by [McKinley, 1961, Cervera and Reid, 1995]

$$dP_r^d = dP_r e^{-(8\pi^2 r_0^2/\lambda^2)} e^{-32\pi^2 D_a t/\lambda^2}, \tag{2.2}$$

where D_a is the ambipolar diffusion coefficient, r_0 is the initial radius of the trail, dP_r is the the echo power in the case of no diffusion and all electrons concentrated on the axis of the trail and dP_r^d is the echo power including diffusion. Integration of (2.2) and applying appropriate phase shifts [Cervera and Reid, 1995] gives the echo power due to the entire trail. It is important to include the attenuation of the meteor echo power due to the the finite velocity of formation effect [Steel and Elford, 1991]. The first exponential in (2.2) results in the immediate attenuation of the received echo power as a result of the finite initial radius of the trail, while the second exponential describes the attenuation of the received echo power as a result of ambipolar diffusion. Thus the echo decay time constant is defined as the time taken for the echo power to decay by a factor e^{-2} (or amplitude decay by a factor of e^{-1}), and is given by

$$\tau = \frac{\lambda^2}{16\pi^2 D_a}. \tag{2.3}$$

Solving for D_a yields

$$D_a = \frac{\lambda^2}{16\pi^2 \tau}, \tag{2.4}$$

which is independent of all radar parameters except wavelength. The result in Jones [1995] indicates a Gaussian initial distribution is in fact not quite correct and that the initial distribution is more correctly described by a dense narrow core and a more diffuse central region. This result however does not affect the "decay part" of (2.2). This result is fundamental to the estimation of meteor diffusion coefficients and the derivation of atmospheric temperatures.

Dyrud et al. [2001] and Hall [2002] have shown that unlike the diffusivity of air which increases exponentially with height, diffusion rates of meteor trails do not vary in the same manner. The results of Dyrud et al. [2001] and Hall [2002] have shown that anomalous diffusion takes place due to electromagnetic and neutral turbulent effects. This is an important aspect of radar studies of meteor diffusion rates and as such will effect temperatures estimated using diffusion coefficients. Dyrud et al. [2001] has shown that diffusion rates are effected above 96 km at mid-latitudes and above 94 km at latitudes greater than 60°. Results from temperature comparisons over the height range of the meteor distribution are presented later, the primary focus being on estimating the temperature at the peak height (accounting

for its annual variation) of the meteor distribution. Hall [2002] has shown that model estimates of the variation in diffusivities between 1-1.5 $m^2.s^{-1}$ between 88 and 90 km. This variation is less than the observed variance in diffusion coefficients used in estimating the average diffusion coefficient used in the determination of temperatures. We next discuss the AOA for meteor trails and highlight the error associated with making such measurements, which forms the motivation for using interferometric techniques.

2.3 Meteor Angle of Arrival Determination

Meteor radars have been used in numerous configurations from Co-axial-Co-linear (Co-Co) arrays [Cervera and Reid, 1995] to observations made with MF radar [Tsutsumi and Aso, 2005] and superDARN systems [Tsutsumi et al., 2009]. Jones et al. [1998] have shown the influence mutual antenna coupling has on meteor angle of arrival (AOA) estimation. The meteor systems used in this study use interferometric receive antenna array configurations as recommended by Jones et al. [1998]. The following derivation follows from the work of Jones et al. [1998] and has been reproduced for the benefit of the reader.

Consider a pair of antennas in a single base-line on the interferometer (Figure 2.2). The phase difference measured between the received signals of antennas 0 and 1 can be written as follows[1]:

$$\phi_{10} = -2\pi\frac{d}{\lambda}\sin(\alpha)$$

re-arranging gives us the expression:

$$\sin(\alpha) = -\frac{\lambda}{2\pi d}\phi_{10} \tag{2.5}$$

Since ϕ_{10} is measured in a range of $\pm\pi$, then α is measured unambiguously in the range $\pm\pi/2$ provided $d \leq 0.5\lambda$. This however leads to the problem of mutual coupling. Mutual coupling is the name given to the process where the current flowing in one antenna induces current to flow in a closely situated antenna. The induced currents introduce the phase error in the received

[1]All subscripts used in the derivation of AOA estimation refer to antenna numbers as defined in Figures 2.2 and 2.3

signals. Suppose the error in α is only due to the error in ϕ_{10}; i.e. there is no uncertainty in d and λ. We can re-write (2.5) as follows:

$$\sin(\alpha + \Delta\alpha) = -\frac{\lambda}{2\pi d}(\phi_{10} + \Delta\phi_{10}). \tag{2.6}$$

By applying the trigonometric expansion and small angle approximation ($\sin(\Delta\alpha) \simeq \Delta\alpha$) to Equation (2.6) we obtain:

$$\sin(\alpha) + \Delta\alpha\cos(\alpha) = -\frac{\lambda}{2\pi d}(\phi_{10} + \Delta\phi_{10}). \tag{2.7}$$

Substituting (2.5) into (2.7) and solving for $\Delta\alpha$ we arrive at an estimate for the error in AOA due to the error associated with the phase measured between antennas.

$$\Delta\alpha \approx -\frac{\lambda}{2\pi d}\frac{\Delta\phi_{10}}{\cos(\alpha)} \tag{2.8}$$

$\Delta\alpha$ is minimised and holds for $d = \frac{n\lambda}{2}$, where $n > 1$ and is a positive integer (i.e. $n \in \mathbb{Z}^+$). This, however, leads us to the problem where there is now an ambiguity in the number of multiples of 2π in the received signal phase estimate. This issue is easily resolved by the use of a third antenna in the base line of the interferometer spaced at a multiple of $\frac{\lambda}{2}$ from the other two antennas. If we look at Figure 2.3 we can write the following expressions for the phases measured on each of the two outer antennas with respect to the inner antenna.

$$\phi_{10} = -\frac{2\pi d_1}{\lambda}\sin(\alpha) \tag{2.9}$$

$$\phi_{20} = \frac{2\pi d_2}{\lambda}\sin(\alpha) \tag{2.10}$$

Now if we add and subtract (2.9) and (2.10) we obtain the following results for our AOA estimate:

$$\sin(\alpha) = -\frac{\lambda}{2\pi}\frac{\phi_{10} - \phi_{20}}{d_1 + d_2} \tag{2.11}$$

$$\sin(\alpha) = \frac{\lambda}{2\pi}\frac{\phi_{10} + \phi_{20}}{d_1 - d_2} \tag{2.12}$$

Equation (2.11) provides us with an accurate estimate for α but is ambiguous due to the multiples of 2π. Equation (2.12) provides us with an inaccurate

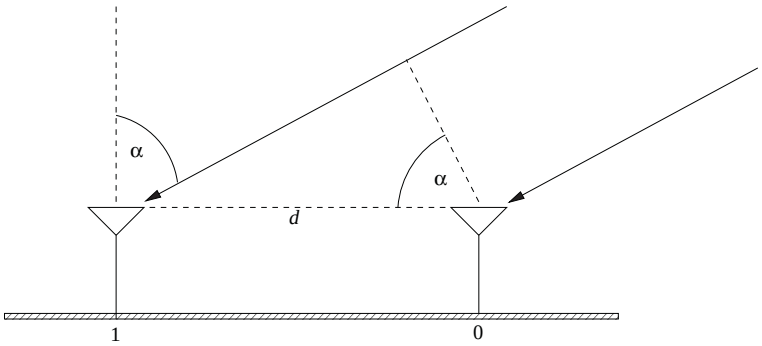

Figure 2.2: A pair of antennas along a common base line of an interferometer. α is the angle-of-arrival of the return signal from the meteor trail.

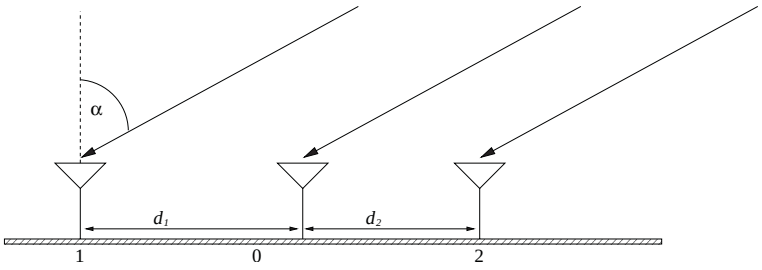

Figure 2.3: A single base line from an interferometer. Both d_1 and $d_2 = \frac{n\lambda}{2}$

estimate for α, but it does enable us to resolve the ambiguity in the multiples of 2π which is present in the solution to (2.11). For example, if we apply the relative spacings used by the meteor systems used in this study, i.e. of $d_1 = 2.5\lambda$ and $d_2 = 2\lambda$, we observe that (2.11) yields an effective spacing of 4.5λ which minimises the error in the phase measurement $\Delta\phi_{12}$ and thus the error in our estimate for α. (2.12) on the other hand yields and equivalent spacing of 0.5λ which, resolves the ambiguity of $2m\pi$ ($m \in \mathbb{Z}^+$) in (2.11). In the next section we discuss how meteor AOA estimates can be used to determine winds in the MLT region.

2.4 Meteor Wind Estimates

As meteors enter the Earth's atmosphere and ablate, they leave in their wake a dust trail which is highly charged. The charge density of the trail is much greater than that of the surrounding atmosphere. This results in a gradient in the radio refractive index of the atmosphere and as such the trail forms a scattering target for electromagnetic signals transmitted by the radar system. The expression for the refractive index is given by

$$n = 1 + 0.373\frac{e}{T^2} + 77.6 \times 10^{-6}\frac{p}{T} - 40.3\frac{N_e}{f^2}, \tag{2.13}$$

where e is the humidity, T is the temperature, p is the pressure and N_e is the electron density. The last two terms in equation (2.13) are the dominating terms in the MLT region as $e \simeq 0$. These trails drift with the mean wind and as such introduce a Doppler shift in the frequency of the radar signal. The magnitude of the shift is given by

$$\Delta f = \frac{2fv}{c} = \frac{v}{\lambda}. \tag{2.14}$$

Wind estimates in the MLT region with meteor radar systems are generated by measuring line of sight Doppler radial velocities (see Figure 2.4). Due to the Earth's rotation, whereby a point of latitude and longitude will be moving toward the meteor stream during the local morning hours and away from the stream in the evening hours, the meteor flux varies throughout the course of the day. This means that the number of meteor detections in a single height-time acquisition bin varies substantially enough such that at certain times of the day there are not enough echoes to determine a reliable wind estimate for small height-time bins. Therefore cumulative measurements over multiple height-time bin acquisitions are required. Time bins of one hour were chosen to increase the number of detections in a single height-time bin to improve the statistical accuracy of wind estimates. This subsequently results in spatially averaged horizontal wind field estimates [Holdsworth et al., 2004]. Estimates of the components of the horizontal wind field (zonal u and meridinal v) are calculated by solving

$$V_r = ul + vm, \tag{2.15}$$

using a two dimensional least squares fit to the measured radial velocity and direction cosines l and m derived from the meteor AOA. The vertical

component w is assumed to be zero when solving for u and v upon the grounds that the vertical component of the wind field averages to zero both temporally (over the time bin) and spatially (over the large field-of-view). From (2.15) it can be seen that only two distinct echoes are required in order to generate solutions for u and v. The analysis software however, utilizes a criteria that a minimum of six echoes are required in order to determine values for u and v in order to maintain a degree of statistical reliability [Holdsworth et al., 2004]. To ensure against suspect wind estimates, the projected radial velocity from individual estimates of u and v are calculated and then subtracted from the actual radial velocity estimate. If the difference between the projected and actual radial velocity exceeds 25 m.s^{-1} then the echo is rejected and the process is repeated until all echoes satisfy this criteria [Holdsworth et al., 2004]. In calculating u and v, the radar generates hourly time bin averages over two kilometre height bins due to the sporadic nature of meteor echo events. The hourly averaged winds are stored along with other parameters including a data quality flag as a "*.vel*" file. Table 2.1 below describes the data quality flags used. The analysis of wind data in this thesis only utilizes wind velocity estimates which have a error=0 flag associated with them.

Error Code	Description
0	Wind velocity estimate is ok
1	Insufficient data to generate reliable wind velocity estimate
3	Wind speed ($\sqrt{u^2+v^2}$) $\geq$ 200 m.s^{-1}

Table 2.1: ATRAD meteor wind velocity error codes. Each wind velocity estimate contained within the analysed wind velocity data file has an associated error code.

The ATRAD meteor analysis software requires a minimum of 4 samples of a underdense echo. We can therefore calculate the minimum duration of the echo required by the analysis software in order to determine the parameters that are returned by the radar. This can be done using the following expression.

$$\text{min. duration} = \frac{1}{PRF} \times CI \times \text{min. number of samples}, \tag{2.16}$$

where PRF is the Pulse Repetition Frequency and CI is the number of Coherent Integrations. For a VTX system operating with a PRF=1960 Hz

and CI=16, this gives a minimum echo duration of 0.0327s. For a STX or STX-II system operating with a PRF=440 Hz and CI=4, this gives a minimum echo duration of 0.0364s.

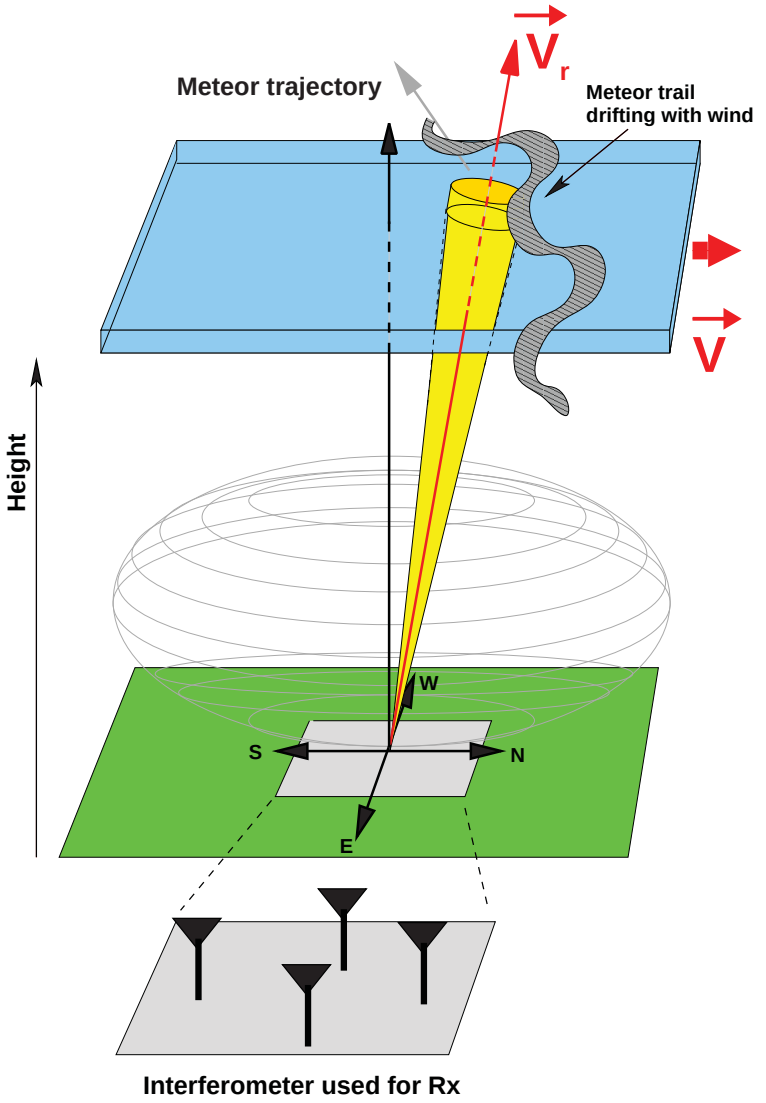

Figure 2.4: A graphic depiction of the detection of a meteor trail and measurement of line-of-sight Doppler radial velocity. The ellipsoid represents the approximate field-of-view of a single receive antenna in the interferometer.

2.5 MF Radar

Medium Frequency (MF) atmospheric radar systems operate primarily using the spaced antenna method of obtaining wind velocity estimates. MF radar systems utilise layers of ionised electrons in the ionosphere as a scattering mechanism for radio waves. The creation of these layers is discussed in Section 1.1.1. The radio waves that are back scattered form a ground diffraction pattern that moves with the motion of the scatterers moving with the background wind. If the scatterers are moving with velocity v, then the ground diffraction pattern moves with velocity $2v$. This is known as the point source effect [Briggs and Vincent, 1980]. See Figure 2.5.

The MF system applies spatial correlation techniques to a minimum of three separate receivers that sample the ground diffraction pattern and its evolution over time in order to generate estimates of the wind field. A full description of correlation analysis techniques can be found in Briggs [1968], Briggs and Vincent [1980], MacKinnon [2001]. In addition to the FCA technique, the BP MF radar also employs another analysis technique for the determination of winds called Imaging Doppler Interferometry (IDI). The IDI technique uses the "single scatterer" criterion whereby it assumes the measured received signal results from a point scatterer. IDI is similar to the meteor technique in that it measures an Angle of Arrival (AOA) and a radial velocity from which the analysis can calculate zonal and meriodional wind components. A detailed description of the FCA and IDI analyses implemented with the ATRAD analysis software that is run on the BP MF radar and Davis MF radar (FCA only) can be found in Holdsworth and Reid [2004a].

The MF radar systems employ a vertically directed beam for measurement of atmospheric winds with a range of beam widths depending upon the system's configuration. For example, the Davis MF system has a beam width (full-width-half-maxima) of $\sim 60^\circ$ (see Figure 3.17) for transmission while the BP MF radar is capable of achieving a beam width closer to $\sim 10^\circ$ if all antennas were to be used for transmission [Holdsworth and Reid, 2004b]. This results in a narrow field of view in comparison to the all-sky technique employed by the meteor radars used in this study and as such the MF winds represent a smaller horizontal spatial average compared with those of the meteor radars. Unlike the sporadic nature of meteors, the ionization scatterers are non-sporadic and as such allow for better temporal resolution (i.e

wind estimates every 2 minutes) as opposed to meteor wind estimates which are put into hourly time bins. As mentioned previously, the source of scatterers is due to the ionization of atmospheric constituents by solar radiation. The combination of the depletion of scatterers at night along with Earth's geomagnetic field results in the variation in the reliability of wind estimates over all range-time bins.

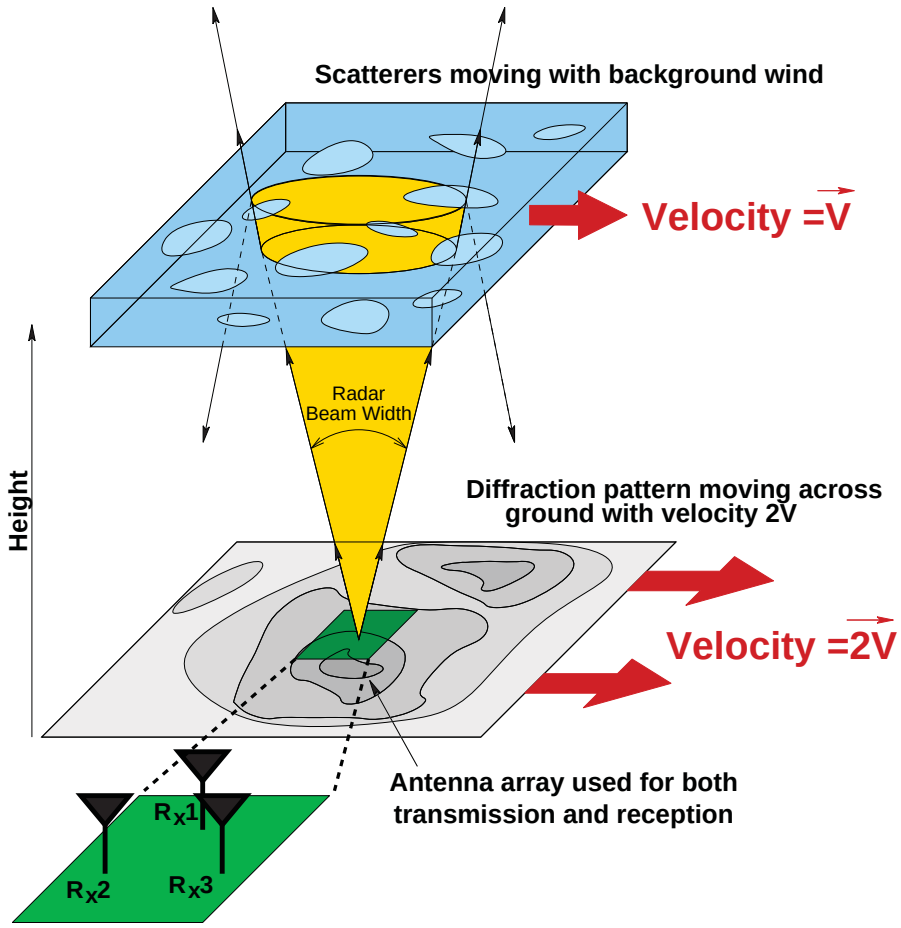

Figure 2.5: Principles of spaced antenna wind measurements. See text for details.

2.6 Satellite Observations

The use of satellites in atmospheric profiling has increased significantly in recent years. Two sources of satellite data are used in comparisons of atmospheric temperatures within this thesis. They are AURA, which is a part of NASA's Earth Observing System (EOS) Microwave Limb Sounding (MLS) satellite, and the Sounding of the Atmosphere using Broadband Emission Radiometry (SABER) instrument aboard the Thermosphere, Ionosphere, Mesosphere, Energetics and Dynamics (TIMED) satellite. Both instruments are limb sounding instruments which obtain remote measurements of atmospheric parameters by observing millimeter- and submillimeter-wavelength thermal emission (radiances) as the instrument field-of-view (IFOV) is scanned through the atmospheric limb from above. Figure 2.6 provides a visual description of the measurement technique. Both instruments are able to generate profiles of the atmosphere for many data products including temperature and pressure, which are the two data products used in this study. Limb measurements are made by both platforms of emissions from various chemical species in the atmosphere that include CO_2, OH, HO_2, H_2O, O_2, O_3, NO and various species of chlorine based molecules.

AURA operates in a sun-synchronous orbit at an altitude of ∼705 km at 98° inclination. The SABER instrument operates in a sun-synchronous orbit at an altitude of ∼625 km at 74° inclination. Both instruments report data products from the lowest few kilometres of the atmosphere (∼10 km) to the middle and upper atmosphere (∼110 km) and operate at differing frequencies which provide various degrees of both temporal and spatial (horizontal and vertical) resolution. Data vertical resolution ranges from ∼1.5 km to ∼7 km and a horizontal resolution of ∼2 km to ∼13 km depending upon which atmospheric constituent is being observed. For more detailed descriptions of the platforms and performance the reader is directed to *http://mls.jpl.nasa.gov* for a document entitled "*An Overview of the EOS MLS Experiment*" and *http://mls.jpl.nasa.gov/data/datadocs.php* which describes the instrument mission, platform and performance of AURA and to refer to *http://saber.gats-inc.com/index.php*, Xu et al. [2006], Kumar et al. [2008], Gracia-Comas et al. [2008], for detailed descriptions of the SABER mission, platform and performance.

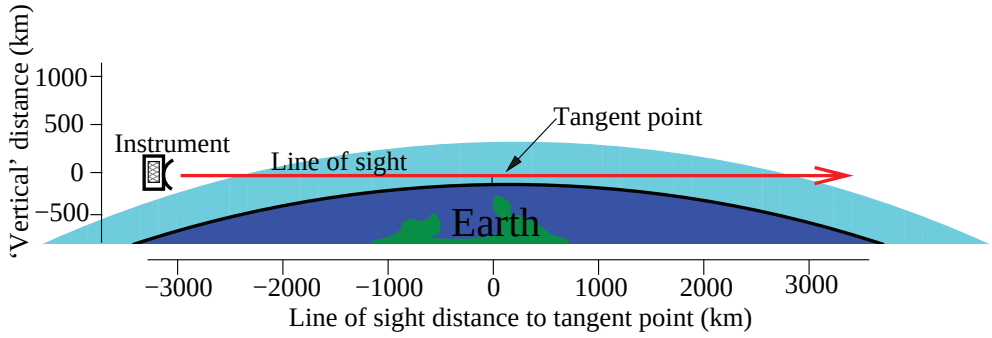

Figure 2.6: The diagram above shows the limb sounding technique. In the case of AURA which is in a 705 km altitude orbit, the line of sight as depicted above would correspond to a tangent height of 50 km. This diagram has not been drawn to any scale.

2.7 Falling Sphere Measurements

Unlike the other forms of measurement contained within this thesis, Falling Sphere (FS) measurements are in-situ measurements of the atmosphere. The technique involves the use of a rocket which delivers the FS to an altitude of approximately 110 km [Lübken and von Zahn, 1991, Lübken, 1999, Lübken et al., 2004]. The FS is manufactured from a metalized mylar material. After release at altitude, the FS inflates to a diameter of one metre and begins to passively fall through the atmosphere whereby it decelerates. A high-precision radar tracks the descent trajectory which is then used with the equations of motion in order to determine atmospheric density (from deceleration) and horizontal winds. Temperature profiles are obtained by integrating the density profile assuming hydrostatic equilibrium. The initial falling temperature ("start temperature" T_0) needs to be taken from some other measurement or model. FS measurements provide for excellent spatial resolution, however they do not provide as good temporal resolution compared with radar observations. This is due to the high costs associated with the rocket observations that generally limits observations to one or two soundings a day over a short observation period [Lübken and von Zahn, 1991, Lübken, 1999].

2.8 Airglow Observations

Airglow observations have been an integral part of mesospheric observations of temperature and gravity wave activity; e.g French et al. [2005], Reid and Woithe [2005]. There are a number of instruments used for the determination of night time O_2 and Hydroxyl (OH) emission layers which include scanning spectrometers and three-field photometers. This thesis makes use of OH rotational temperatures that were derived from observed emission spectra of the OH layer. The hydroxyl layer has a mean height of ∼87 km with a mean thickness of ∼8 km [French and Burns, 2004].

OH emissions at Davis Station are observed with a 1.26 m Czerny-Turner scanning spectrometer. 250 μm entrance slits provided a resolution of ∼0.16 nm with a $\sim 5.3^\circ$ field-of-view in the zenith [French and Burns, 2004]. A more in-depth description of the instrument can be found in Williams [1996]. A description of the operational modes of the instrument can be found in French and Burns [2004], Phillips et al. [2004], French et al. [2005]. The transitional probabilities presented in Langhoff et al. [1986] which are in strong agreement with those found by French et al. [2000] are used in the determination of rotational temperatures. The method for the determination of rotational temperatures is detailed in Burns et al. [2002]. Corrections are applied to transitional probabilities as well as accounting for contributions from aurora and moonlight and are detailed in French and Burns [2004]. Sample temperatures are derived as the weighted average of temperatures from three possible ratios $P_1(2)$, $P_1(4)$ and $P_1(5)$ emission lines. The weighting factor used in the process is the statistical counting error (based on the error in estimating each line intensity) [French and Burns, 2004]. The harmonic fit parameters used within in this study were derived from calculated temperatures over the period 1995 to 2007.

OH emissions at Buckland Park are observed with a three-field photometer (3FP). The 3FP uses 3 GaAs photomultipliers with a telecentric lens and filter wheel which contains 6 filters; three 750 nm and three 557.7 nm filters with 3 nm passbands. The arrangement can be seen in Figure 2.7. One set of filters is used for OH emissions while the other is used for OI emissions. OH observations are made for 20 seconds on the minute before the wheel is rotated and OI acquisition occurs for 20 seconds starting on the next half minute. The resulting data consists of three time series of the OH intensities sampled simultaneously in three fields with a temporal resolution of 1 minute

and likewise with the OI data set. The instrument shutter is closed every 15 min to allow for a dark count to replace the 730 nm measurements, which would normally occur on the minute. The centres of the three fields are separated by ∼13 km at heights near 97 km for OI observations and by 12 km at heights near 87 km for OH observations [Reid and Woithe, 2005]. Similar to Davis, temperature estimates are made through the use of transition probabilities with emission spectra. The harmonic fit parameters used in this study were derived from temperature estimates made using this technique.

In the next chapter we discuss the meteor systems in more detail and highlight the development of the high-powered meteor radar system at BP.

Figure 2.7: A plan view of the filter wheel of the three-field photometer showing the two filter sets and the field projection at the observed airglow heights. Filters 1, 3, and 5 (all 730 nm) are in use then filters 2, 4, and 6 (all 587.7 nm) are then in use. A particular filter is always matched to the same photomultiplier, so that a filter-photomultiplier combination always represents the same channel. Diagram and description sourced from Reid and Woithe [2005].

Chapter 3

Radar Hardware

3.1 VHF Meteor Radar System

Meteor observations using radar techniques can be classified into two distinct groups; mono-static (backscatter) or bi-static (forward scatter) radars. In the mono-static case, both the transmit and receive systems are co-located whereas a bi-static system employs the use of separately located transmitter and receive systems[1]. Multiple VHF meteor radar systems were used as a part of this study. The radars are located at Darwin, Northern Territory, Buckland Park (BP), South Australia, and two at Davis Station, Antarctica. All meteor radar systems used are mono-static radar systems. The systems were manufactured by ATmospheric RADar systems (ATRAD) with some developmental work on the BP system undertaken in conjunction with the University of Adelaide. All observed parameters and analysis of observed parameters are derived from the received radio frequency (RF) signal that results from the interaction between the meteor ablation trail and the transmitted RF signal.

The primary purpose of the meteor radar system is to profile the atmosphere in terms of wind velocity and temperature in the MLT region over the range of the meteor height distribution [Steel and Elford, 1991]. The observed fundamental parameters are: angle-of-arrival (AOA), echo decay time (τ), range to the trail, and Doppler radial drift velocity (V_r). From these parameters, further analysis can be applied in order to determine wind

[1]The criteria for a bi-static radar system is one in which the distance between the transmitter and receiver is greater than the distance between the transmitter and the target

velocity estimates for the zonal (u) and meriodional (v) components and the ambipolar diffusion coefficient for the meteor trail. All parameters are determined by an analysis PC, which analyses the raw data set produced by the acquisition computer.

3.1.1 Radar Operation

The radar operates on the basis of transmission and reception of RF information. The main components of the system are:

- Analysis and acquisition computers,
- Multichannel transceiver,
- Pulsed transmitter,
- Transmit and receive antennas.

The radar is operated through a graphical user interface on the analysis PC. The analysis PC runs the Slackware flavour of the Linux operating system and its primary role is in the analysis of the acquired raw data and to provide a user interface to configure the radar's transmit and receive parameters. The analysis computer is also responsible for producing data plots which can be transferred to a web server via FTP protocol such that the radar's status and performance can be monitored remotely.

Once the experiment parameters have been saved in a experiment configuration file this information is transferred to the radar acquisition PC which is responsible for providing the parameters to the transceiver, radar timing control and communicating with the radar hardware for any faults in the system. The acquisition PC is responsible for the conversion of received analogue In-phase (I) and quadrature-phase (Q) signals into a digital representation for the analysis PC as described in Section 3.1.3.

3.1.2 Interferometer

Historically, the use of arrays of antennas (antenna spacing $\lesssim 0.5\lambda$) for receiving have been used; e.g. Cervera [1996]. Jones et al. [1998] has shown that this approach leads to uncertainties introduced into the AOA estimates due to mutual coupling affects between antennas. The results described in

Jones et al. [1998] detail the degree of uncertainty introduced into AOA estimates for receive antennas arranged with spacings of 0.5λ. From these results it was decided that the spacing configuration described in Jones et al. [1998] would provide the best AOA estimates and as such an interferometer with a spacing configuration as prescribed by Jones et al. would be used. The interferometer consists of 5 receiving antennas that can be arranged to form either a T, L or a cross (see Figure 3.1).

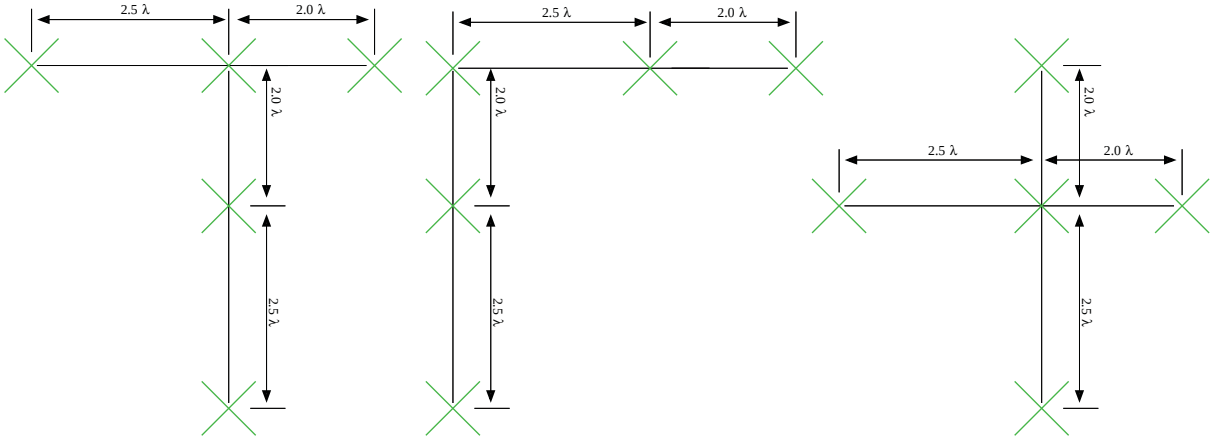

Figure 3.1: Meteor radar interferometer variations. The Darwin system uses the T-shape while the BP and Davis systems use the cross-shape. The green crosses designate receive antenna locations. The Darwin and BP systems use crossed dipole receive antennas while the Davis systems utilised only linear dipole receivers until the summer 2007-2008 expedition.

The analysis software is able to determine AOA estimates based upon the phases measured by receiving antennas located along common base lines. See Section 2.3 for the derivation expressions used to determine the unambiguous AOA.

3.1.3 Acquisition System

The acquisition system for the meteor radar system converts the received RF signal into a digitized representation that can be analysed by the analysis computer. The acquisition system consists of two main components, a 6 channel transceiver and the acquisition computer. The acquisition computer is a standard PC with Pentium processor, running the Microsoft Windows 2000 operating system, and an A4D1 14-bit data acquisition board which digitizes the signal from the transceiver for processing. The receiving component of the transceiver processes the received RF signal in the analogue domain into a signal suitable to be digitized and analysed.

In standard meteor radar observations only 5-channels from the transceiver are used in the detection of meteor echoes. A sixth channel can be used for the centre antenna of the interferometer for Faraday rotation experiments, however this is outside the scope of study of this thesis. Consider a single receiver channel. When an RF signal is received on an antenna, as described in Section 3.1.2, the signal received enters the receiver front-end amplifier (see Figure 3.2). At this point the signal is filtered by a wide-band band-pass filter to help remove background noise and then amplified by approximately 20 dB. The signal is then passed to the down-converter where it is amplified, band-pass filtered and then passed to a mixer which produces intermediate frequency (IF) signals. A reference signal ($f = 135$ MHz) generated by the RF oscillator is provided to the mixer which produces new signals at frequencies equal to the sum and difference of received signal frequency and frequency of the reference signal. This process is known as hetrodyning. The hetrodyning process is used in order to improve the frequency selectivity process along with boosting the amplitude of the received signal since the amplitude of the received signal on the antenna is of the order of microvolts. Boosting the received signal is also necessary in order to improve the Analogue-to-Digital (A/D) conversion. According to Cervera [1996], hetrodyning was used to convert signals to an IF which was much lower than the original frequency, however this led to problems with aliasing. In the current VHF meteor systems, the received signal frequency is increased at the IF stage which maintains the frequency selectivity of the receiver system while not introducing aliasing issues.

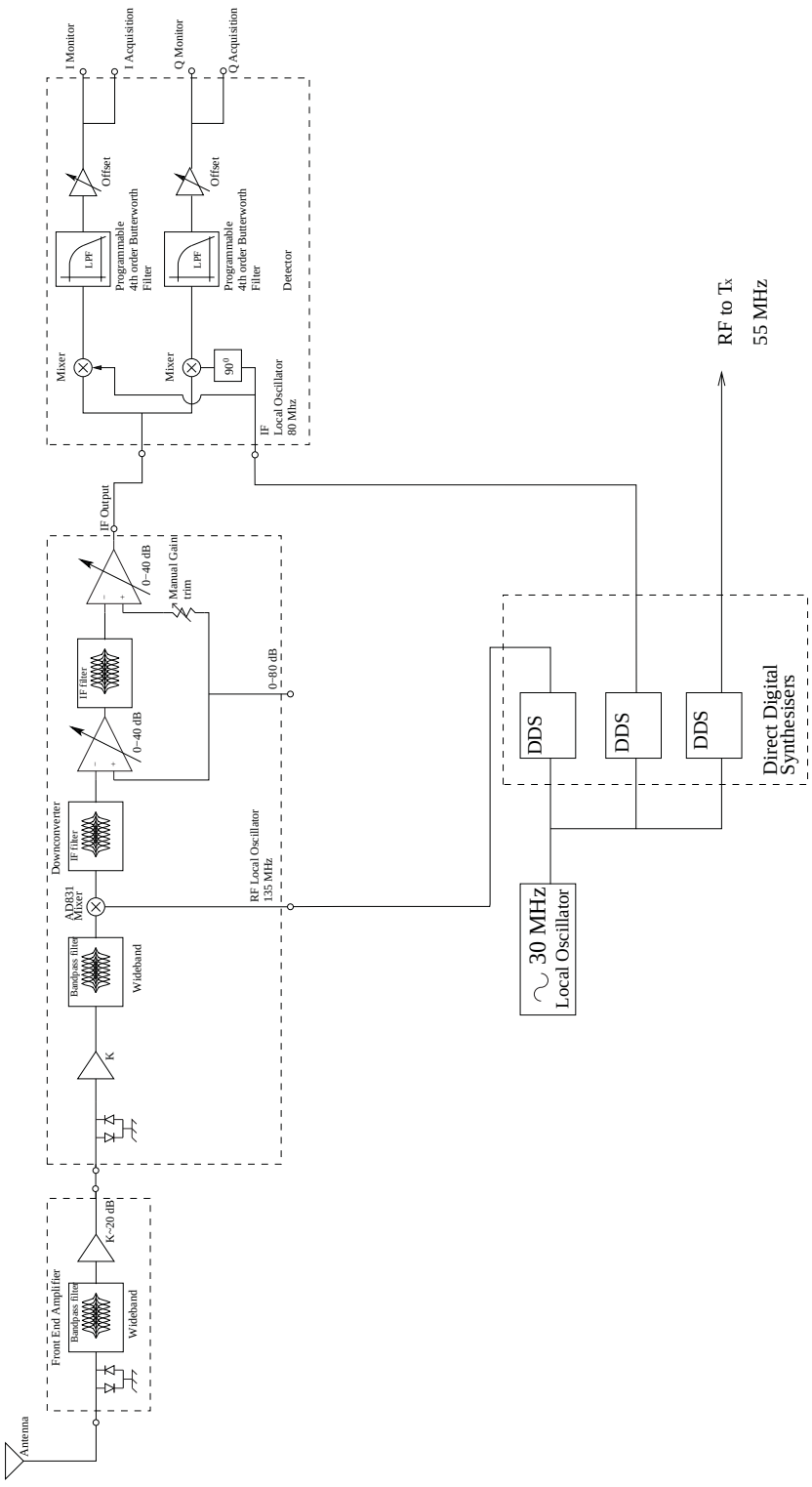

Figure 3.2: Analogue signal processing component of radar transceiver. The above block diagram shows how a received signal is processed by the transceiver and is converted to base-band I and Q signals. The I and Q are then digitised by the acquisition PC and then sent to the analysis PC. Refer to the text in Section 3.1.3 for a full description.

In Figure 3.2 the mixing process by the AD831 produces new signals at 190 MHz and 80 MHz. The new 80 MHz IF signal is passed through an IF filter (bandwidth$\sim$ 1-2 MHz) which blocks all mixed products (see Figure 3.3). The new IF signal is amplified by a gain controllable amplifier with a range of 0-40 dB. The signal is then passed to a second stage IF filter and amplifier with the same characteristics as the first stage. The gain of each stage after the mixer can be adjusted via the radar configuration software to fit the appropriate experimental parameters. The output signal from the down-converter is then passed to the detector stage.

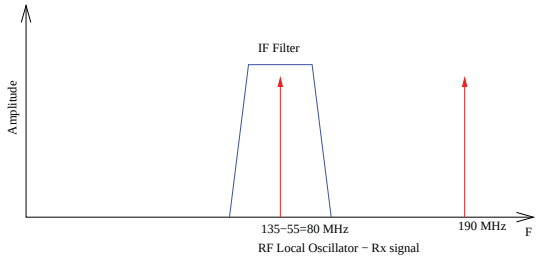

Figure 3.3: First stage IF filter process in down-converter.

The detector stage involves a similar mixer stage as performed in the down-converter as well as additional filtering, and offset gain adjustment. The offset gain adjustment removes any DC bias present in the signal. The first stage of the detector involves passing the signal to two separate mixers. Each mixer is provided with a reference signal (f = 80 MHz) with one of the reference signals being in quadrature (90° out of phase) with respect to the other. The result of which are in-phase (I) and quadrature-phase (Q) signals being produced at frequencies equal to the sum (f = 160 MHz) and difference (f = 0 Hz) of the first stage IF signal frequency and the reference frequency. These signals are then passed through a fourth order programmable Butterworth filter with a variable cut-off frequency between 18.1-404 kHz (in 64 steps). See Figure 3.4. This produces both $\pm$ 10 V I and Q signals which can be measured on the front panel of the transceiver for each channel. The I and Q signals produced by the transceiver are also then passed to an attenuator that reduces the maximum possible voltage to $\pm$ 2V, which is then fed to the data acquisition card. The I and Q signals are produced in order to deduce relative amplitude and phase information between each channel's received signals, as well as the signal amplitude (the

magnitude of the I and Q vector).

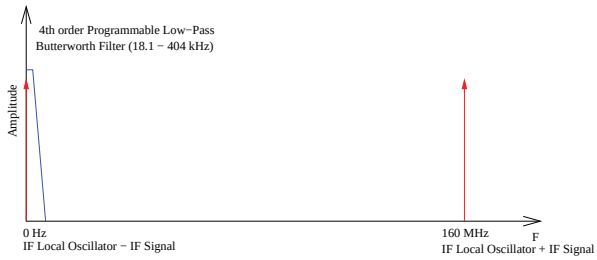

Figure 3.4: Detector IF and filtering process.

The data acquisition card takes the reduced I and Q signals from transceiver to a multiplexer board which performs a simultaneous sample and hold on the signals. This is then passed through to a 4:1 multiplexer and is then passed to the A4D1 board where it is filtered and passed to a 14-bit Analogue-to-Digital (A/D) converter. Only 12-bits out of 14 are used as the last two bits have been found to introduce noise into the digitized signal. The 12-bit digitized signal is shifted by 4-bits in software to convert it into a 16-bit representation, thus increasing the dynamic range (DNR) to $\simeq 96.32$ dB[2]. We thus have $2^{16bit} = 65536$ possible values which can then be used to represent values in a range from -32768 to +32767. This forms the basis of the averaging process which can be adjusted in the radar configuration software by changing the number of coherent integrations (CI) of the signal. If CI=1, then the 12-bit signal is simply converted to a 16-bit representation by a 4-bit shifting operation. If CI= n, then each of the n 12-bit representations is averaged as follows:

$$\text{average} = \begin{cases} \text{CI} = 1 & \text{then 12-bit} \rightarrow \text{16-bit;} \\ \text{CI} = n & \text{then } \frac{1}{n}\sum_{i=0}^{n}(\text{12-bit})_i \times 16. \end{cases}$$

A block diagram of this process can be found in Figure 3.5

[2]The Dynamic range for a digitized signal represented by b-bits can be calculated using the expression $DNR = 20\log_{10}\frac{(2^b-1)\delta}{\delta} \simeq b20\log_{10}2 = 6.02b$ dB

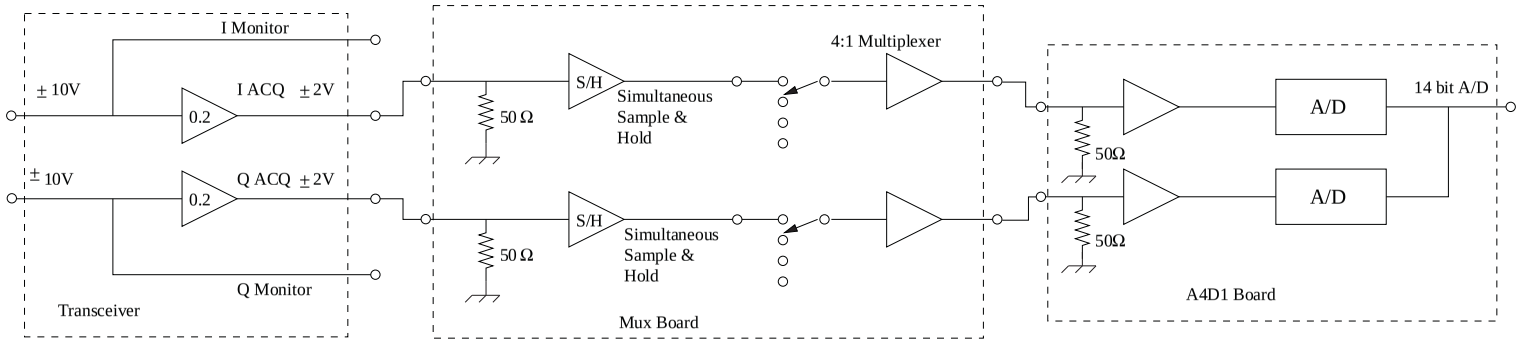

Figure 3.5: Digital signal processing component of radar acquisition system. Contained within the first box to the left is the output stage of the radar transceiver. This produces the ±2V I and Q signals that are fed to the data acquisition card as well as providing the ±10V I and Q monitor port signals on the front panel of the transceiver. The mux board in the second (middle) box povides the input to the data acquisition card. If the number of CI=1 then the signal is passed directly through to the A4D1 board where the analogue signal is digitised. If the number of CI is greater than 1, then the signal is averaged as described in the averaging expression in Section 3.1.3 and then converted to a 16-bit representation for processing by the analysis computer.

3.1.4 Darwin System Description

The Darwin meteor radar has a first generation solid-state transmitter (STX-I) manufactured by ATRAD. The table below has a summary of the system's characteristics.

Parameter		Units
Carrier Frequency f:	33.2	MHz
Carrier Wavelength λ:	9.04	m
Effective Pulse Width (EPW):	3600	m
Pulse Width (EPW$\times 2/c$):	24.0	μs
Pulse repetition frequency (PRF):	430	Hz
Pulse type:		Gaussian modulated
Sampling Interval:	2	km
Maximum range:	347	km
Range Aliasing:	No	
Sampling range start:	70	km
Sampling Range finish:	314.8	km
Peak power:	8	kW
Coding:	4-bit Complimentary	
Duty Cycle:	4.13	%
Interferometer Configuration:	T	Shape

Table 3.1: Typical radar parameter set used on the Darwin radar. The duty cycle is calculated using $c^{-1} \times 2 \times (\text{Pulse Width}) \times PRF \times (\text{No. coded bits}) \times 100$, where c is the speed of light. See Figure 3.6 for a graphical depiction of the interferometer layout.

The STX-I system utilises three solid state transmit modules which combine together to give a nominal peak output power of 8 kW (4 kW per output from the combiner). The outputs of the three transmit (Tx) modules are combined via a 3:2 combiner system which directly feeds the crossed dipole Tx antenna with an in-phase (I) signal and quadrature (Q) phase signal (i.e. $\Delta\phi_{QI} = 90°$). This results in the Tx antenna radiating circularly polarised radiation. The Q is achieved by inserting an extra length of RG-213 cable cut to an electrical length of $\frac{\lambda}{4}$. The radar system receives return echoes on a 5 antenna interferometer. The interferometer is arranged in a T-shape and

can be seen in Figure 3.6. A description of how the interferometer works can be found in Section 3.1.2

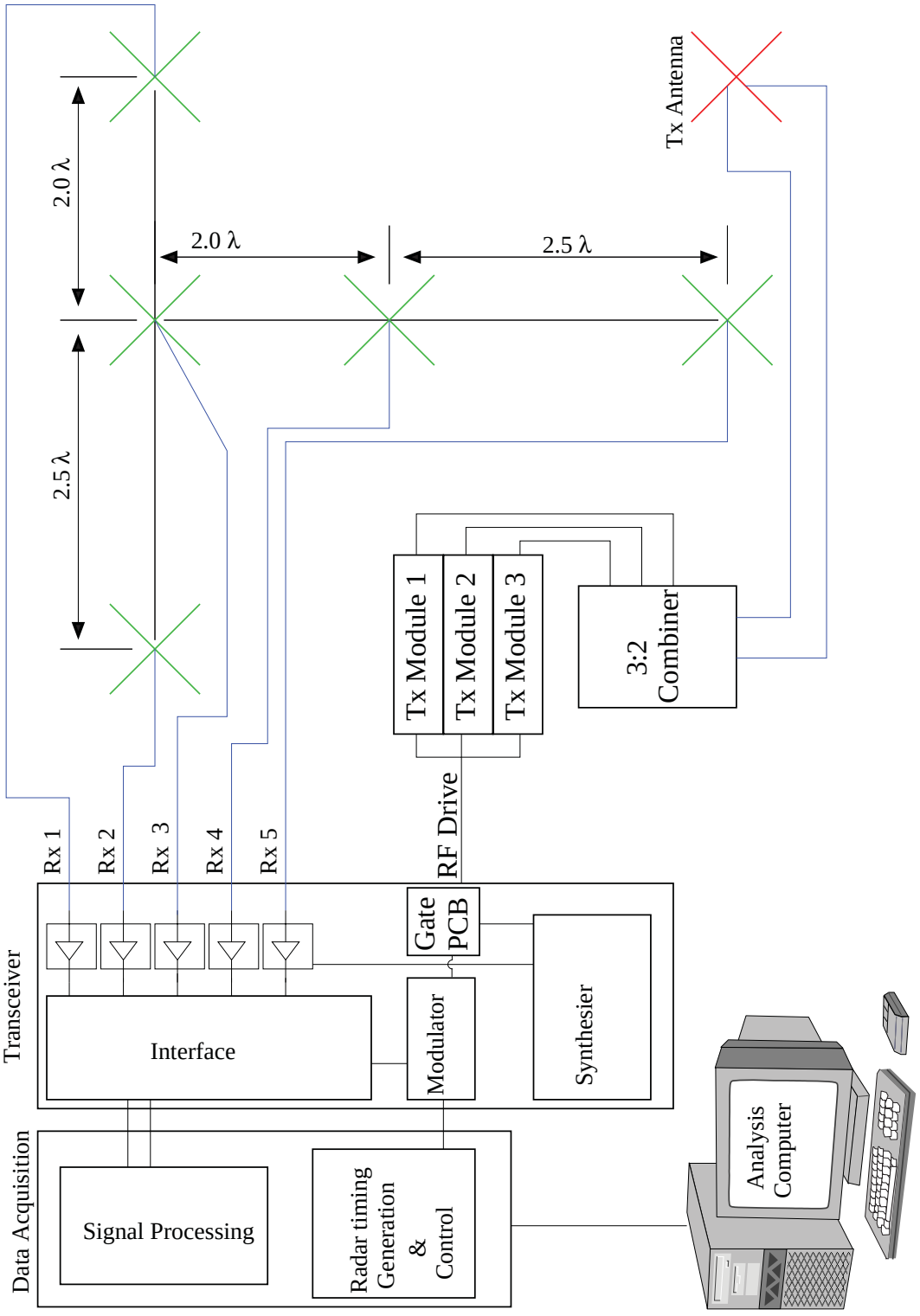

Figure 3.6: Darwin meteor radar block diagram. The green crosses represent the receive antennas and the red cross represents the crossed dipole transmit antenna.

3.1.5 Antennas

The transmit antenna is essentially two, two-element Yagi antennas arranged in a cross. Each two-element Yagi has a half-wave dipole driven element and a reflector. The driven element is fed directly from the output of the 3:2 combiner via RG-213 coaxial cable. The matching of cable impedance to antenna impedance is achieved via a gamma-match arrangement.

The gamma-match is designed to match the antenna's input impedance to the characteristic impedance of the feed cable. For RG-213 this is 50Ω. The gamma-matched system can be understood via Figure 3.7. The outer conductor of the coaxial cable is attached at the middle point of the $\frac{\lambda}{2}$ dipole as the RF voltage at this point is zero. The centre conductor is tapped off on one side of the driven element at the point where the impedance of the dipole is approximately equal to the characteristic impedance of the feed cable. A tunable capacitor is placed in series with the centre conductor in order to tune out any excess reactance thus presenting a 50Ω input impedance to the feeder cable. The position of the tap point is varied using a sliding clamp arrangement. The capacitor is simply a sliding aluminium rod inside a slightly larger aluminium tube. Both are insulated from one another. The centre conductor of the coax is attached to the rod. The capacitance can be altered by sliding the rod in or out from the tube. The rod insertion point is insulated using heat shrink material.

The receiving antennas are cross dipole antennas which utilise a delta-match system so they have circular polarisation receive capability. The delta-match is in essence two gamma-match arrangements which are combined via a 90° quadrature-splitter microcircuit. The receive antennas are connected to the receiver front-ends via RG-213 cable for the Darwin system and LMR-400 for the BP system.

3.1.6 Buckland Park Hybrid System Description

The BP system underwent two stages of evolution during the course of this study. The first system configuration used a valve transmitter (VTX) and was a hybrid combination of a Stratospheric-Tropospheric (ST) and meteor radars. The second stage of evolution was the use of an STX-II transmitter. The STX-II is the second generation of solid state VHF transmitters manufactured by ATRAD and is completely modular in design and functionality.

The unique hybrid combination between a ST and meteor system allows

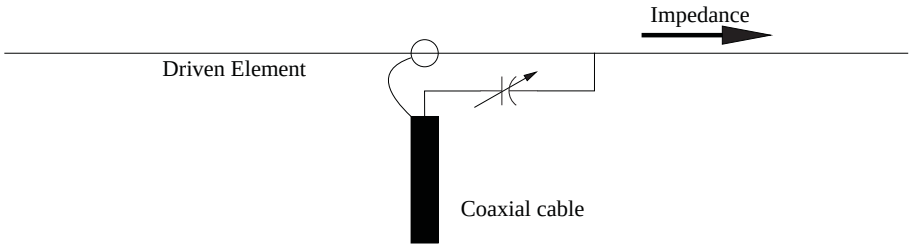

Figure 3.7: The above diagram is a pseudo circuit diagram of the gamma-match arrangement. A half-wave dipole's impedance is zero in the middle and increases moving towards the end points. The gamma-match is tapped (connected) at the point along the driven element that has an impedance of approximately 50Ω and the push-rod variable capacitor is used to tune out any excess reactance at the tap point.

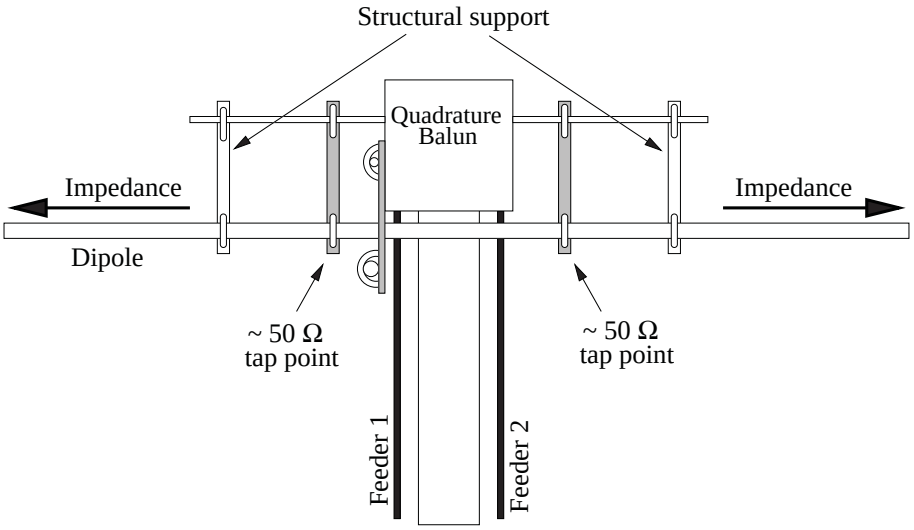

Figure 3.8: The delta-match is essentially two gamma-match systems combined vi a quadrature microcircuit splitter.

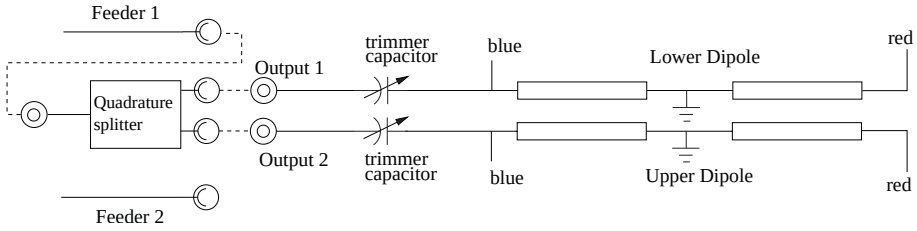

Figure 3.9: Quadrature balun electrical layout. The trimmer caps are present to tune out any excess reactance once the $\sim 50\Omega$ tap point has been found.

the meteor system to take advantage of the high output power capability that is normally associated with ST systems. The meteor component of the hybrid system consists of a receive interferometer and crossed dipole transmit antenna while the ST component consists of an array of 144 3-elements Yagi antennas. The ST component operates using Doppler Beam Steering (DBS) techniques. In the VTX configuration the beam steering unit also handles the switching between meteor and ST modes of operation. ST operations are outside the scope of this study and no further detail is provided. The main functional difference between the VTX and STX-II transmitters is that the VTX has 6 Tx outputs where as the STX-II has 4 (Figures 3.10 and 3.11); 2 for feeding the meteor transmit antenna directly and 2 for ST operation. The 2 outputs for ST operation are combined via the second generation 1:2 splitter-combiner (see Chapter 5) and then split 6-ways with the 1:6 splitter to provide the 6 Tx channels for ST operation.

In the first generation of the VTX hybrid system, only a single VTX Tx module was used for the Tx antenna. This meant that the beam steering unit was only required to switch a single output from the VTX from the ST transmit path to the meteor transmit path. In the second generation upgrade, when all six output channels from the VTX were to be fed to the meteor transmit antenna, a new splitter combiner system was required and is described in Section 3.1.8. A table of the system's characteristics can be found below.

Parameter	VTX	STX-II	Units
Carrier Frequency f:	55	55	MHz
Carrier Wavelength λ:	5.45	5.45	m
Effective Pulse Width (EPW):	2275	7200	m
Pulse Width (EPW$\times 2/c$):	15.17	48.0	μs
Pulse Repetition Frequency: (PRF)	1960	430	Hz
Pulse type:			Gaussian modulated
Sampling Interval:	2	2	km
Maximum range:	75	345.2	km
Range Aliasing:	Yes	No	
Sampling Range Start:	75	70	km
Sampling Range Finish:	300	314.8	km
Peak Power:	75	40	kW
Coding:	None	4-bit Complimentary	
Duty Cycle:	2.97	8.25	%
Interferometer Configuration:	Cross	Shape	

Table 3.2: Typical BP experiment parameters. See Figure 3.10 for a graphical depiction of the interferometer layout.

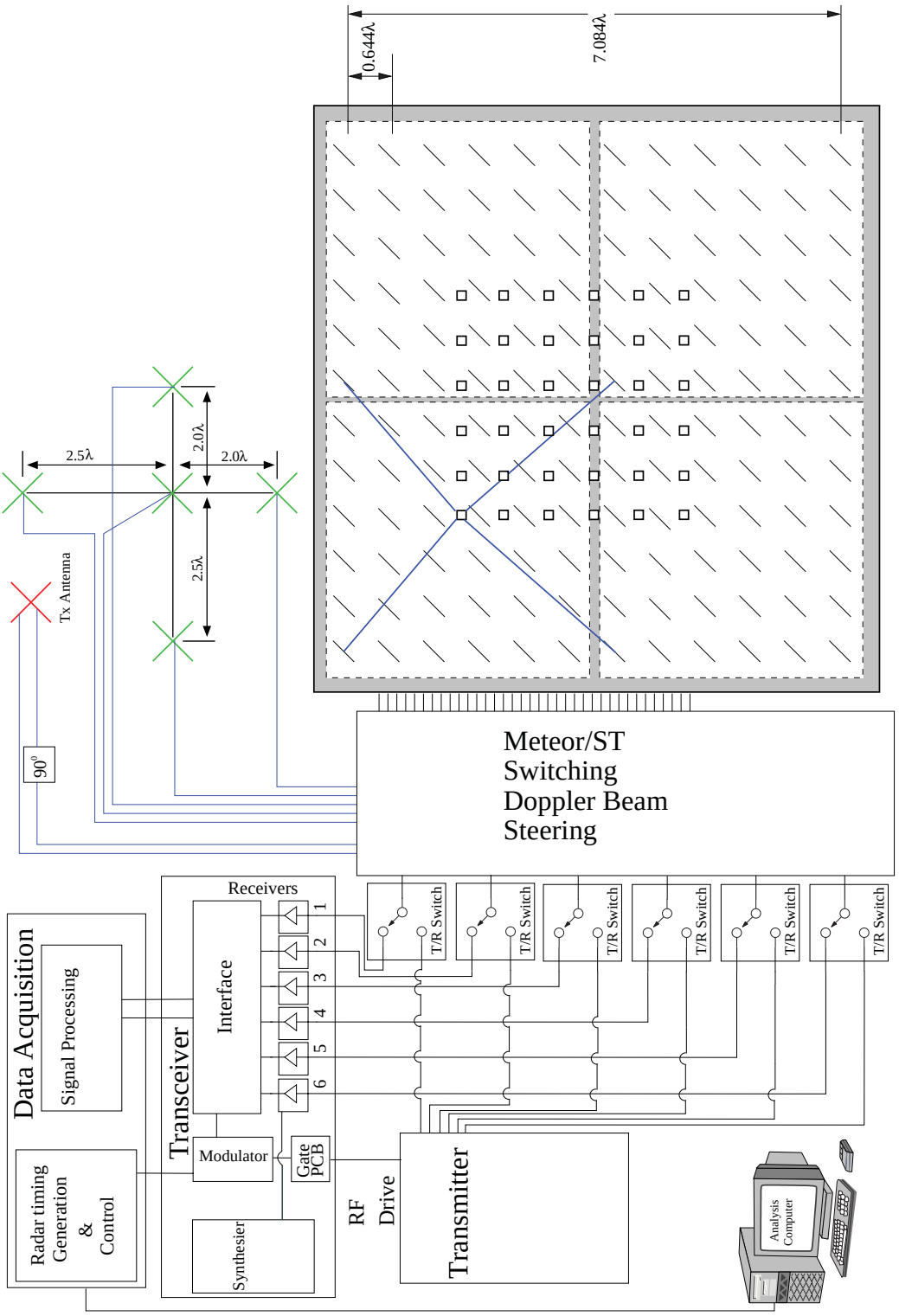

Figure 3.10: BP hybrid VTX Meteor/Stratospheric-Tropospheric (ST) radar system. The system selects between transmission and reception on either the meteor antennas or the ST array. The ST DBS array can also be used for meteor studies but this is beyond the scope of this study.

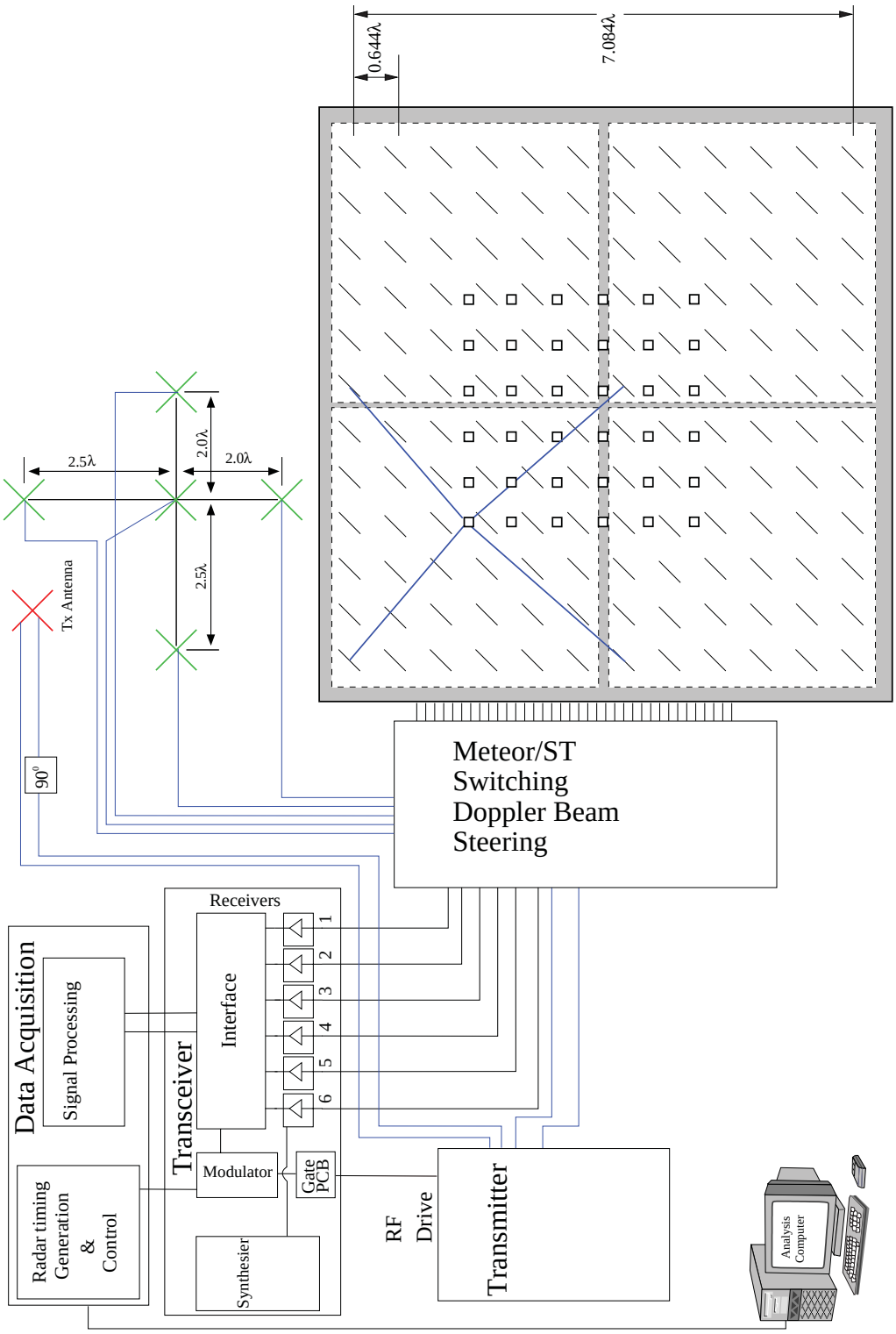

Figure 3.11: BP hybrid STX-II Meteor/ST radar system. Beam steering is achieved by feeding different phased currents to the six rows or columns of antenna feeders (square array of square dots in diagram).

3.1.7 Antennas

The receive antennas used for the system are the same design as those used for the Darwin meteor receive antennas; the only difference is the lengths of the antenna elements due to the different frequency of operation. The system required the design of a new transmit antenna system that would be capable of handling the power delivered to it from the VTX transmitter. Normal linear cross-dipole antennas associated with meteor radar systems like the Darwin system are not capable of handling the high power produced by a VTX system. There is also the issue of matching the feed-line impedance to the impedance of the antenna feed-point. A simple gamma-match arrangement would not be suitable due to the large voltage potentials at the feed-point, which would result in arcing in the gamma-match due to its design. It was also desirable to improve the gain of the transmit antenna system.

There were two stages of evolution in the development of the Tx antenna for the hybrid system. The first stage was to select an antenna and matching system that would be cable of handling the power. The next step was to utilise the design formulae given in Green [1966], Balanis [1997], and also outlined in Appendix A, as an initial guide to designing the antenna. Once the initial dimensions were established, the antenna was constructed and simulated within the EZNEC modeling environment to establish performance characteristics and overall tuning of the antenna.

Once a design was finalised, the antenna (dubbed "Gen-1") was then prototyped by Broadband Propagation with components capable of utilising the power from a single Tx module from the VTX with a nominal peak output power of 20 kW. The cable runs and hair-pin matching system were constructed from LMR-400 cable as well as utilising "N-type" connectors which met the 20 kW specification. Despite the computer simulation showing feed-point impedances of $Z_1 = 202.6 + j4.4045\Omega$ and $Z_2 = 207.8 + j3.026\Omega$, a minor tuning modification was required as the feed-point impedance was not exactly 200Ω on the prototype. This meant that the 4:1 hair-pin balun would not step-down the feed-point impedance to exactly 50Ω and hence provide a match to the feed-line impedance. The tuning was achieved via a simple tuned circuit provided by Broadband Propagation. A more detailed description of the design, modeling and fabrication process of the antenna can be found in Chapter 4.

Once Gen-1 proved to be successful in its role as an all-sky transmit

antenna for a meteor system, the next stage was to increase the antenna's power handling capability. This meant that both the connectors for the antenna and cable runs were required to be upgraded from "N-type" to "7/16" connectors as well as upgrading the cable used in the balun and cable runs to LMR-600. This antenna was dubbed "Gen-2". The nominal peak output power from the VTX is 80 kW. This meant that when split by the 1:2 splitter to provide I and Q transmit channels, the LMR-600's 40 kW peak power rating would be capable of delivering the power to the antenna.

3.1.8 High Power Splitter Combiner System

A ST system only requires six separate transmit lines for operation in order to feed the 144 antennas and perform beam steering functions. As such there has been no requirement to combine the six outputs from the VTX transmitter for ST operation. With the advent of Gen-2 and the requirement of combining the six outputs from the VTX into two to feed the meteor antenna, extra hardware was required in order to accomplish this. ATRAD provided a 6:1 combiner which meant that a 1:2 splitter was required to be designed and fabricated. Initially a proposed quadrature splitter (see Figure 3.12) was to be used. The quadrature splitter is a 4-port network device that provides an input port and two output ports (I and Q) with output port 2 (Q) in quadrature (90° out of phase) with respect to port 1 (I). The tuning of the circuit proved to be quite difficult and the design was abandoned in favour of a simpler design which could be tuned more easily. The quadrature component required could be more accurately achieved through the use of an extra $\lambda/4$ of cable.

The design selected for use as the 1:2 splitter was based upon a Wilkinson power divider. The standard Wilkinson 2-way power divider is a 3-port network device. The standard layout can be seen in Figure 3.13 below. The dumping resistor located between ports 1 and 2 was replaced with a Gysel modification due to the high-power involved in the event of a mismatch on either of the output ports. A full description of the design of the splitter can be found in Chapter 5.

The first generation splitter-combiner was accidentally damaged beyond repair after fine tuning of the VTX transmitter Pre-Amplifier (PA) modules. Initially the VTX PA modules when combined together produced a peak output power of 53 kW. This was due to the fact that the peak amplitudes

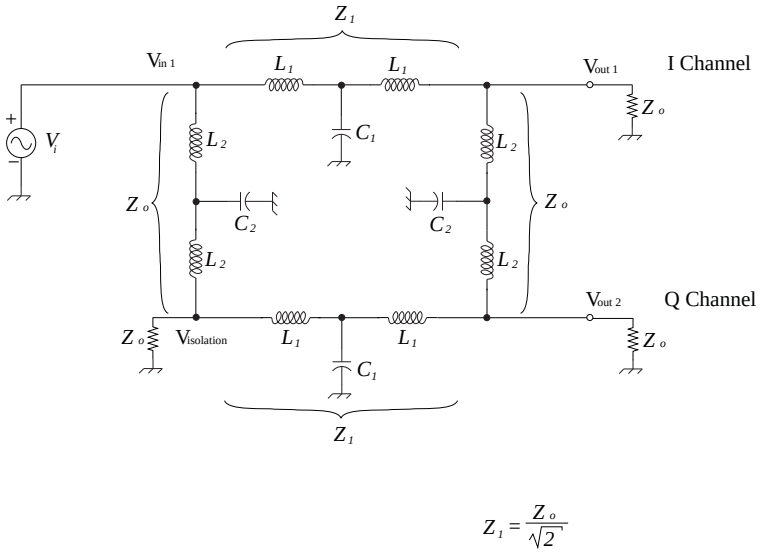

Figure 3.12: Quadrature splitter circuit diagram.

Component	Value	Units
Z_0	50	Ω
Z_1	35.35	Ω
L_1	102.31	nH
L_2	144.69	nH
C_1	81.87	pF
C_2	57.89	pF

Table 3.3: Quadrature splitter component values. L and C values were calculated at 55 MHz using $\omega L = Z$ and $\frac{1}{\omega C} = Z$ where Z is the impedance of the particular branch line.

and phases of each PA relative to the others were not well tuned. After tuning of the PAs, the peak combined power from the VTX was 73 kW ($\sim$1.9 kV) which exceeded the breakdown voltage for the LMR-900 cable connecting the 6:1 combiner and 1:2 splitter. The second generation combiner design was similar to the first generation, however the capacitors used in the quarter wave sections combined to give a larger than required value. Tunable inductors were placed in parallel with these capacitors such that the excess capacitance could be tuned out and a better tuning achieved.

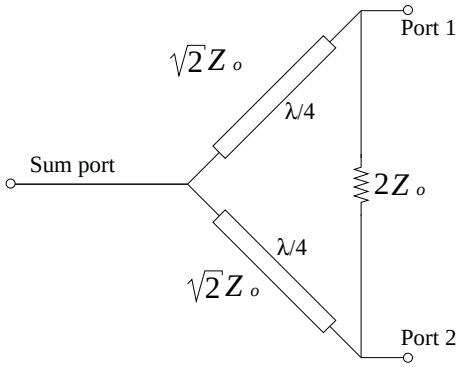

Figure 3.13: Standard Wilkinson power divider.

3.1.9 Buckland Park MF Radar

The Buckland Park MF radar is an array of crossed half-wave dipoles which is approximately 1 square kilometre and operates at a frequency of 1.98 MHz. The array consists of 89 individually accessible north-south and east-west aligned half-wave dipoles. The array was upgraded between 1991 and 1995 such that it could be operated in a Doppler as well as Spaced Antenna (SA) mode. The transmitting system consists of three solid-state modules. The PA modules in transmitters 1 and 2 produce 2.5 kW nominal power each thus providing a total output power of 25 kW from each transmitter. The PA modules in transmitter 3 produce 5 kW nominal power each providing a total output power of 50 kW. The three transmitters can be operated individually or combined to give a total RMS peak envelope power of 100 kW. Each transmitter channel is connected to three dipoles of the antenna array which can also be used for reception through the use of T/R switches. The radar data acquisition system (RDAS) contains 16 receiver channels. The signal processor utilises 12-bit digitisation, which can be increased to 16-bit through the use of coherent integrations. The radar is controlled via a DOS based (acquisition) PC which creates raw data acquisition files that are transferred to a Linux (analysis) PC where it is queued for analysis. For a more detailed description of the MF radar system see Cervera and Reid [1995], Reid et al. [1995], Holdsworth and Reid [2004a,b].

The parameters for typical BP MF observations are listed in Table 3.4 and the layout of the antenna array can be seen in Figure 3.14.

Parameter	Day	Night	Units
Carrier Frequency f:	1.98	1.98	MHz
Carrier Wavelength λ:	151.5	151.5	m
Effective Pulse Width (EPW):	4500	4500	m
Pulse Width (EPW$\times 2/c$):	30	30	μs
Pulse Repetition Frequency: (PRF)	100	20	Hz
Pulse type:			Gaussian modulated
Sampling Interval:	2	2	km
Max Range:	1498	7490	km
Range Aliasing:	No	No	
Sampling Range Start:	50	50	km
Sampling Range Finish:	158	158	km
Peak Power:	92	92	kW
Coding:	None	None	
Duty Cycle:	0.2	0.2	%
Polarisation:	O	E	

Table 3.4: Experiment parameters. Day mode runs between 05:00 and 19:00 LT and night mode operates between 19:00 and 05:00 LT.

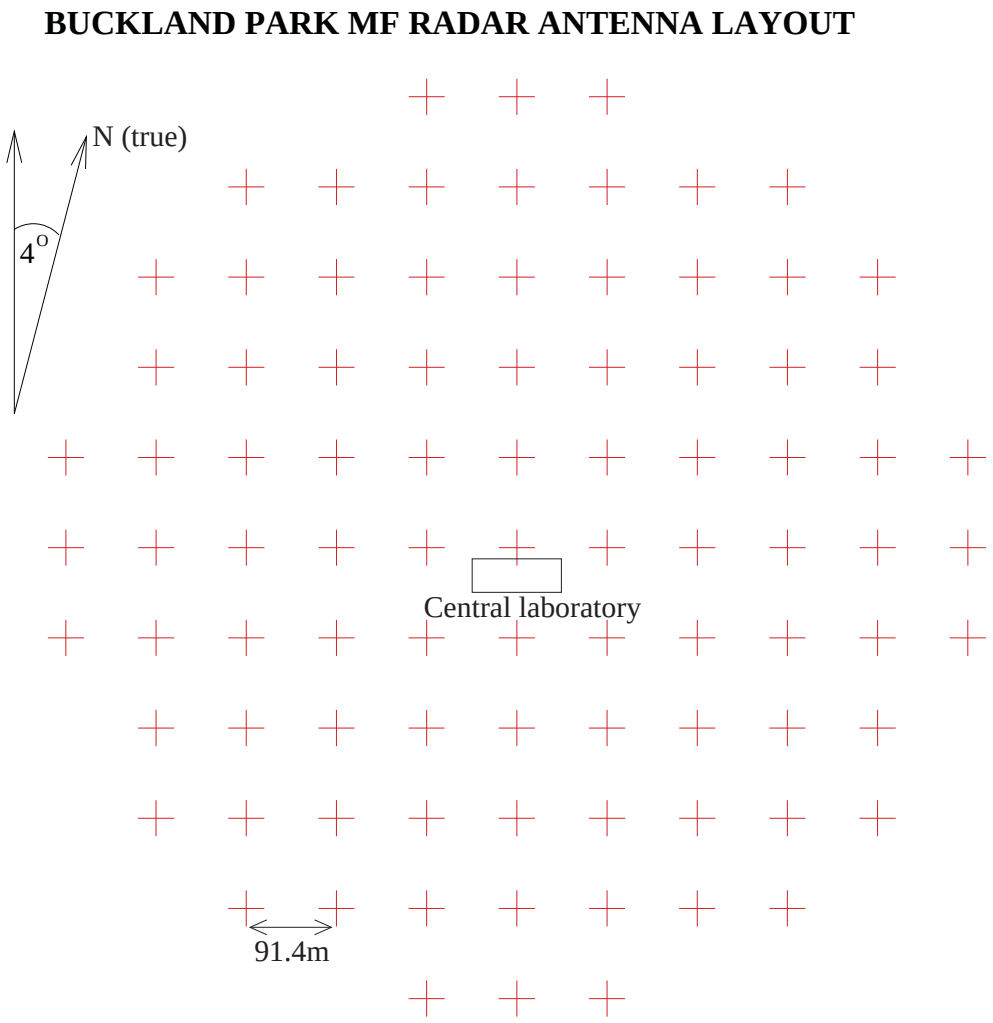

Figure 3.14: The Buckland Park MF Radar layout. The dipole lengths are approximately 75m.

3.1.10 Davis Station Meteor Radar Systems

Davis Station, Antarctica, has two meteor systems that are similar to the Buckland Park and Darwin meteor systems. There is a hybrid 55 MHz MST meteor system as well as a dedicated 33.2 MHz meteor system. The hybrid system differs from the BP system in that the MST array is a spaced antenna array (as opposed to a Doppler array at BP) and the meteor system utilises a lienear crossed dipole with gamma-match arrangement for the transmit antenna and 2 element Yagi antennas with a folded driven element for the

receive antennas for the interferometer. A toroidal balun arrangement is used for matching the receive antennas. The interferometers for both the 55 MHz and 33.2 MHz meteor radar systems are arranged in a cross shape. See Figure 3.1 for a graphical depiction of the interferometer layout. The Davis 55 MHz meteor system only uses one output PA module from a VTX transmitter. The transmit parameters for the Davis 55 MHz system are very similar to those listed in Table 3.2 although the meteor observations are interleaved with ST observations. The 33.2 MHz meteor system is similar to the Darwin system in that it uses a STX-I transmitter, however linear polarised receive antennas were used up until 2007/08. The receive antenna design was a 2-element Yagi with a folded driven element which can be seen in Figure 3.15. The system was installed during the summer 2004/05 expedition. The Davis 33.2 MHz meteor system was run with similar parameters to the Darwin 33.2 MHz system. See Sections 3.1.4 and 3.1.6 for tables of system parameters.

In the summer period, the 55 MHz system runs for a 55 sec duration of minutes 2 and 4 of a 6 minute experimental sequence. During the winter period the 55 MHz system runs meteor mode for 55 seconds of minutes 3 and 5 and for 35 seconds late in the first minute of a 6 minute experimental sequence. The 33.2 MHz meteor system is operated in a continuous meteor observation mode.

Figure 3.15: The Davis 33.2 MHz meteor radar receive antenna. Photograph by Daniel McIntosh. This photo was taken during the summer 2004/05 expedition while tuning antennas in the receiving array. In an unconventional means of tuning the antenna, the distance between the driven element and reflector was 1 cm greater at the ends of the dipoles than at the center. This enabled a perfect $50 \pm 0j\Omega$ match. NEC simulations showed that the difference in reflector spacing would not impact on the polar diagram of the antenna.

3.1.11 Davis Station, Antarctica MF Radar

The Davis MF radar consists of a square transmitting array with 3 separate crossed dipole receive antennas. The system consists of 16 2 kW solid-state transmit modules which feed four half-wave dipole transmit antennas arranged in a square. See Figure 3.16. This gives a peak transmit power of 32 kW or an average power of 60 W with the paramters listed in Table 3.5. Each parallel pair of dipoles are fed in quadrature with respect to the perpendicular pair. The resulting polar diagram for the transmit antennas can be seen in Figure 3.17. The site layout can be seen in Figure 3.16. Each dipole is a half-wavelength at 1.98 MHz ($\sim$ 75m). The receive antenna array is in the shape of an equilateral triangle with spacings of 180m. The radar is operated by alternating between O and X mode polarisations.

Parameter		Units
Carrier Frequency f:	1.98	MHz
Carrier Wavelength λ:	151.5	m
Effective Pulse Width (EPW):	3200	m
Pulse Width (EPW$\times 2/c$):	21.3	μs
Pulse repetition frequency (PRF):	100	Hz
Pulse type:		Gaussian modulated
Sampling Interval:	2	km
Maximum range:	1498	km
Range Aliasing:	No	
Sampling range start:	40	km
Sampling Range finish:	108	km
Peak power:	32	kW
Coding:	none	
Duty Cycle:	$\leq$0.3	%
Polarisation:	O and X mode	

Table 3.5: Davis MF radar experiment parameters.

Figure 3.16: The Davis MF radar layout. Map courtesy of Dr. Damian Murphy, Australian Antarctic Division, Channel Highway Kingston, Tasmania.

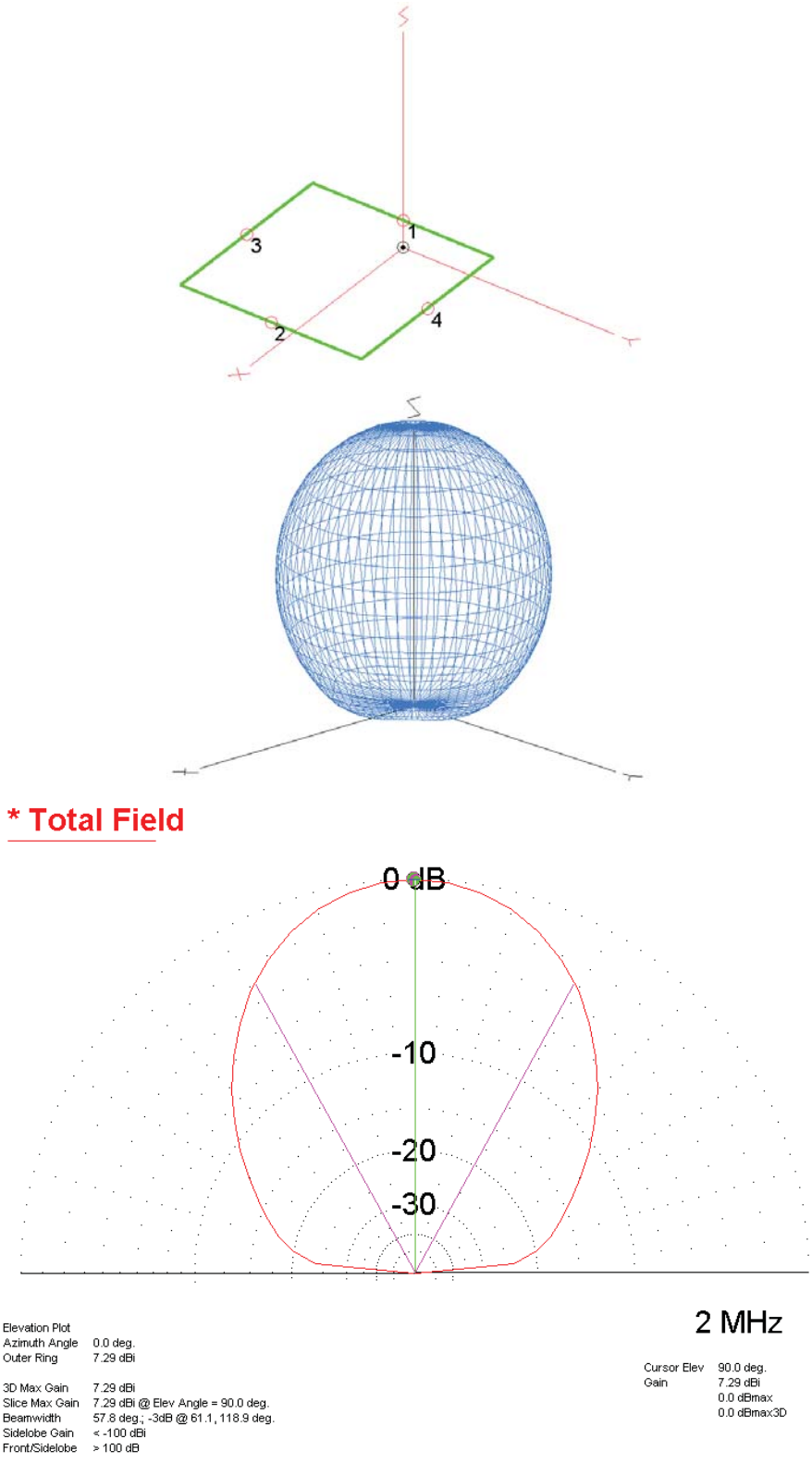

Figure 3.17: The Davis MF radar transmit antenna and polar diagram. The transmit antenna system was simulated with EZNEC with the dipoles placed 11 m above a realistic ground plane. Antennas 3 and 4 were fed in quadrature for circular polarisation.

Chapter 4

High Powered Transmit Antenna Design

One of the driving forces behind the development of meteor radar is the increase in the number of detectable meteor echo trails in order to improve the number of statistical samples present. While the number of echoes detected is strongly dependent upon the frequency of observation, due to Australian government legislation a simple change of operational frequency is not always permitted. As such an increase in transmitted power along with antenna gain is the only option available. This has inspired the development of an antenna capable of handling and transmitting the necessary power to accomplish this. The antenna design of choice is a crossed-folded dipole with a hair-pin balun matching system. The motivation for this choice of antenna was to have an all-sky transmit antenna as opposed to directional Yagi antennas which would have produced azimuthal gaps in the transmission field-of-view. The crossed-folded dipole antenna consists of essentially two two-element Yagi antennas with the driven element being a folded dipole and the reflector being a normal linear $\lambda/2$ dipole. The two Yagi antennas are oriented mutually orthogonal to one another such that they form a single crossed-dipole antenna.

The dipoles used for the antenna were initially designed to be half-wave dipoles (in free-space) with the reflectors being 5% longer than a half-wave dipole. The increase in reflector length adds a marginal amount of inductance in that region in order to reflect the electromagnetic (EM) radiation directed towards it from the driven folded dipole. The design equations for the antenna can be found in Appendix A. After modeling the antenna at 55 MHz with EZNEC, the overall dimensions for the antenna were modified

such that the antenna's radiation characteristics were near isotropic in the presence of a reflecting ground plane, and the feed-point impedance of each folded dipole was reduced from 300 Ω (that for a single folded dipole in free-space) to approximately 202 (± 2)$+j4$ (± 0.5)Ω. This enables the use of a 4:1 hair-pin balanced-to-unbalanced (balun) transformer. According to simulation results this should provide an SWR of 1.024 (± 0.009) for feed-point 1 and an SWR of 1.042 (± 0.009) for feed-point 2 at 55 MHz.

4.1 EZNEC Modeling Results

After extensive modifications of the initial design for the antenna, the optimum theoretical design shown in Figure 4.1 yielded the results shown in Table 4.1.

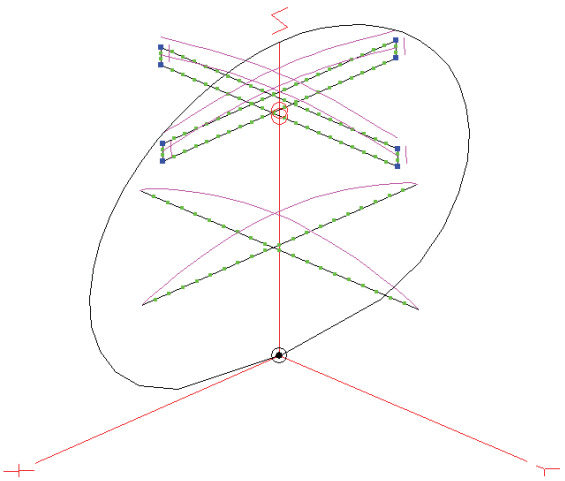

Figure 4.1: The EZNEC folded crossed-dipole model with 2D zenith far-field pattern. The final antenna was constructed with round ends for the driven element. Two models were constructed, one with square ends and the other with approximated rounded ends. There was no difference between the simulation results of the two models and as such all development work was carried out using the model depicted above.

Parameter	Feed point 1	Feed point 2
Volatge (V)	$202.7\angle 1.14^0$	$207.9\angle 0.83^0$
Current (A)	$1\angle 0^0$	$1\angle 90^0$
Impedance	$202.6 + j4.4045\ \Omega$	$207.8 + j3.026\ \Omega$
SWR 50 Ω @ 55 MHz	4.045	4.158
SWR 200 Ω @ 55 MHz	1.024	1.042
Power (W)	202.6	207.8
Total applied power (W) to antenna	202.6 + 207.8	410.5

Table 4.1: Antenna feed-point parameters. Feed-point 1 corresponds to the dipole in the Y-Z plane and feed-point 2 corresponds to the dipole in the X-Z plane.

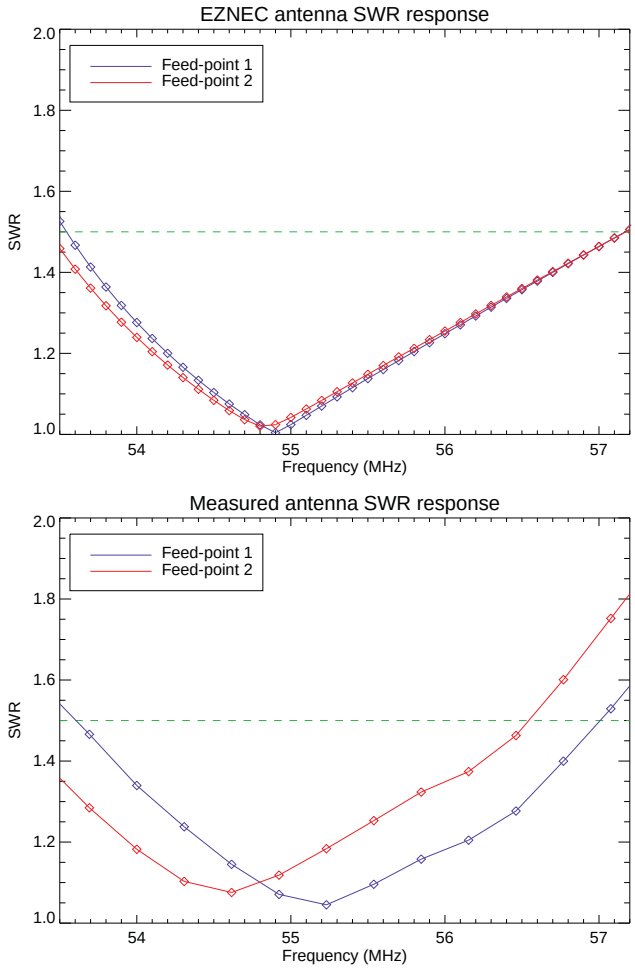

Figure 4.2: The SWR response of the antenna. The top plot shows the results of the EZNEC modeling of the antenna SWR response. The bottom plot shows the first measured SWR response which was conducted at Broadband Propagation's manufacturing facility. The antenna has an acceptable SWR across an operational bandwidth of approximately 3 MHz (53.7 MHz $\rightarrow$ 56.7 MHz) according to the measured values. The measured response curves were obtained using a temporary tuning circuit consisting of a trim-pot capacitor and wound inductor. The final product had a slightly better bandwidth and minimum SWR. The green dashed line represents the imposed SWR threshold performance indicator imposed on the antenna.

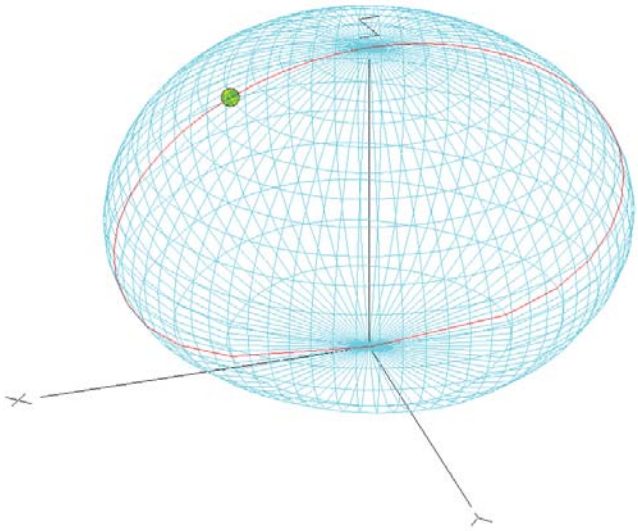

Figure 4.3: The antennas far-field radiation pattern in 3D. The antenna's maximum gain is at 0° from zenith. Although maximum gain is desired between 45° and 60° from zenith, a gain 5.12 dBi at 45° and 3.4 dBi at 60° from zenith was achieved. This proved to be the optimum arrangement for gain and radiation characteristics to meet both tuning and meteor observation requirements.

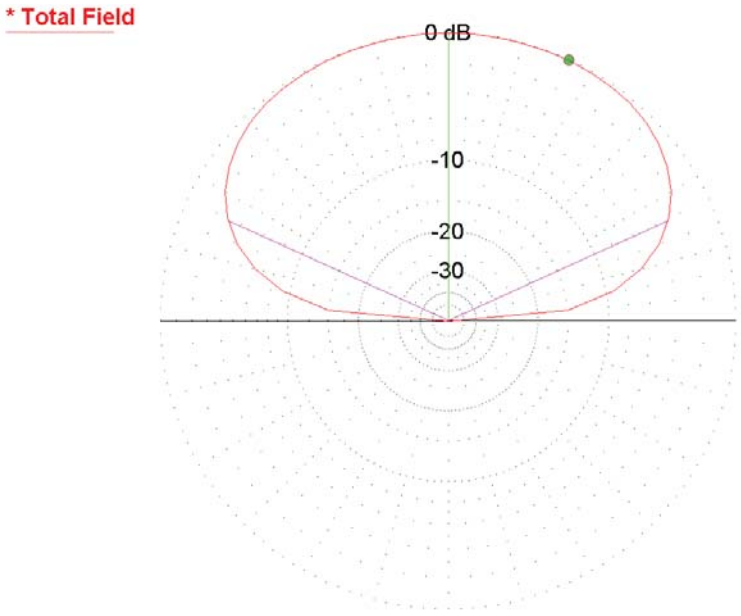

Figure 4.4: The 2D far-field radiation pattern in the direction of maximum radiation. The green line shows the direction of maximum radiation and the purple lines shows the angle of the 3 dB points.

4.2 Schematics for Assembly

The schematics for assembling the antenna can be seen in Figures 4.5 to 4.8. The vertical mounting boom should be between 2.0 and 2.5 m in length to allow for both stability and extra room to move the antenna elements for tuning purposes. The antenna elements can be constructed out of either aluminium or stainless steel. Stainless steel is preferential in arctic type climates where there is a substantial snow fall. The difference in conductivity between the two materials is less than 1 part in 10^6. The steel cross-hatch components in Figure 4.6 are mounted in the middle of the upper arm of the folded dipole inside the clamping mechanism as well as at the midpoint of both reflectors. These components serve as both electrical contact mechanisms as well as enhancing the rigidity of the antenna elements. The folded-dipole at the feed-point is cut and a plastic spacer is placed in place of the tubing in order to form the two feed-points. See Figures 4.9 and 4.10.

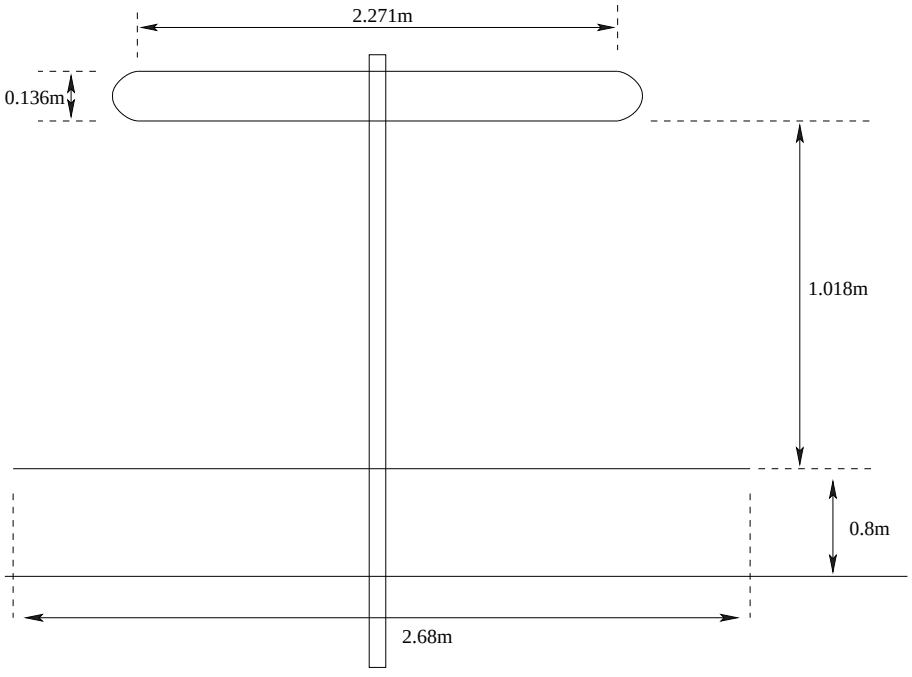

Figure 4.5: Dimensions for construction of crossed-dipole antenna.

Parameter	Dimension (m)
Folded dipole length	2.271
Reflector length	2.68
Diameter of tubing	0.03175
Fold spacing	0.136
Radius Of Curvature (ROC) of fold	0.068

Table 4.2: Antenna dimension parameters

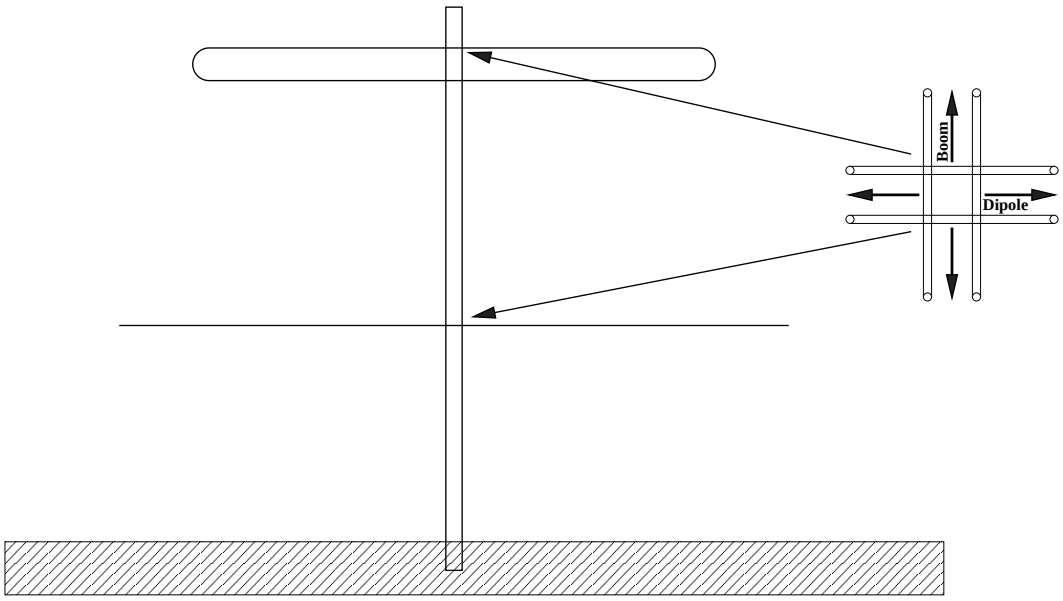

Figure 4.6: Cross-hatch dipole stabaliser and placement points.

4.3 Matching System

A hairpin balun in conjunction with an LC matching circuit is used at the feed point to match the feed point to 50 Ω. The hairpin balun provides a 4:1 impedance transformation converting the antenna's approximate feed-point impedance from 200Ω to 50Ω thus allowing 50Ω LMR-400 or LMR-600 coaxial cable to be used to feed the antenna. The feed point of the antenna did not quite tune to 200Ω with variation of element spacing, hence the requirement for the LC matching (designed by Broadband Propagation) inside the balun box to tune out excess reactance. The antenna can be

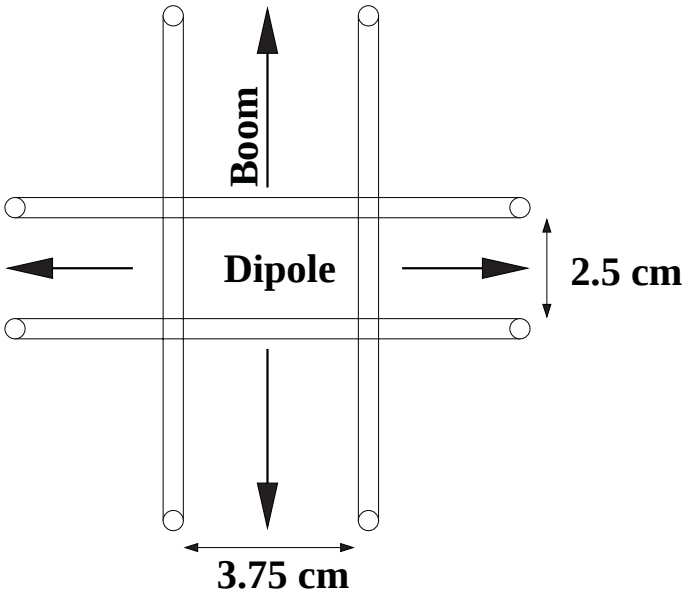

Figure 4.7: Dimensions for the stability hatch.

precisely tuned by varying the spacing of the turns in the coil inductor and carefully trimming the capacitive tuning stub. See Figure 4.11.

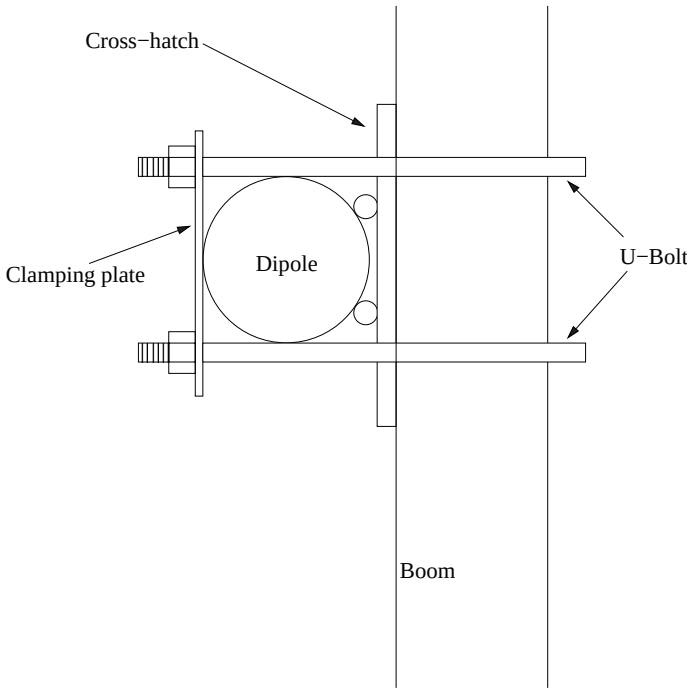

Figure 4.8: This diagram shows how the elements are secured to the boom.

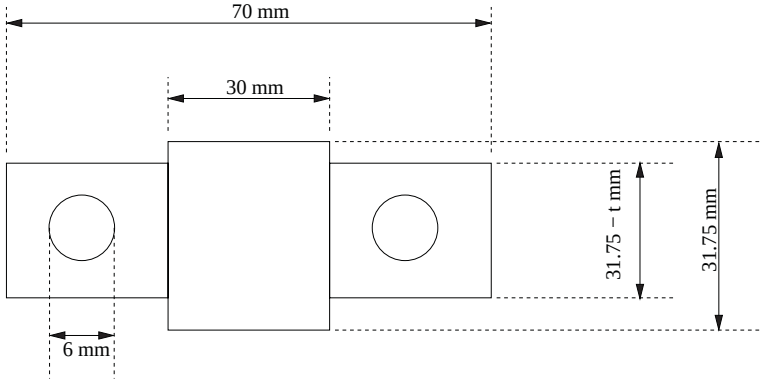

Figure 4.9: Feed-point spacer dimensions. t is the thickness of the metal.

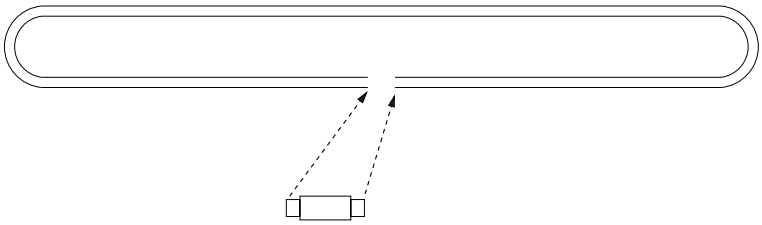

Figure 4.10: Location of the feed-point spacer.

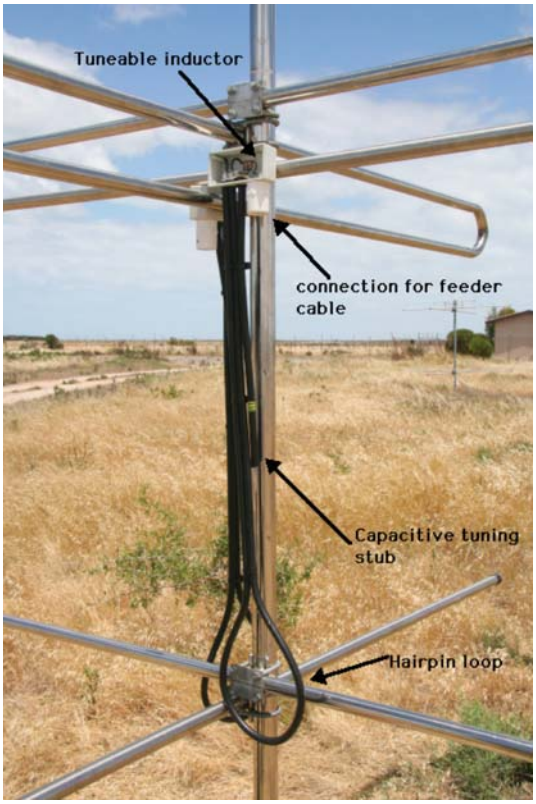

Figure 4.11: The key components to the matching system are highlighted in the photograph. Photograph by Daniel McIntosh.

Figure 4.12: Close up of the balun mounted via 2 bolts that connect directly to the feedpoint. Photograph by Daniel McIntosh.

Figure 4.13: The finished product. Photograph by Daniel McIntosh. One of the receive antennas can be seen in the distance to the left of the brown hut.

4.4 Summary

The goal was to design and construct an all-sky transmit antenna for a meteor radar which would be capable of handling the large amount of power required at 55 MHz in order to increase the number of observed meteors. The antenna itself went through two stages of evolution; the first was to gauge its performance and to provide a stop gap while a 1:2 splitter-combiner could be developed, which would be required for high-powered operations. While the design proved to be not 100% optimal and requiring an ancillary tuning circuit to provide accurate impedance matching, it removed the requirement for further prototyping of the design in order to obtain accurate matching with the use of only the hair-pin matching system. The goals of designing an antenna capable of handling the full power capability of the VTX transmitter along with improving the antenna gain over existing linear crossed dipole antennas were met. The subsequent results of improving the transmit antenna gain and power radiation capability can be seen by the echo rate curves in Chapter 6 and the echo rate plots for BP in Chapter 7. In the next chapter we discuss the design and evolution of the high-powered 1:2 splitter-combiner required to feed the antenna as part of the high-powered meteor operations with the VTX transmitter.

Chapter 5

Splitter-Combiner for Buckland Park ST/High-Power Meteor System

In order to operate the 55MHz BP Radar in high-powered mode, all of the six Tx modules from the VTX transmitter are required. For this purpose a 6:1 combiner constructed by ATRAD was employed. In order to satisfy the requirements for circularly polarized radiation, this combined output from the VTX was then split into two equal outputs by way of a high powered 1:2 splitter-combiner which was designed specifically for this purpose.

5.1 The Design

The basic design of the device is a Wilkinson 2-port power splitter. A 2-port Wilkinson power splitter has a single input/output port called the Sum port and two symmetrical output/input ports with a dumping load connected between these two ports. See Figure 3.13. The impedance at the "Sum" port is defined by the characteric impedance of the feeder cable to be connected to that port. In this case Z_o=50Ω. There is a minor difference between the design used and that of the Wilkinson splitter. The standard Wilkinson splitter utilises a dumping load of impedance $2Z_o$ between ports 1 and 2 in the event there is a problem with either of the two ports. In low power designs this dumping resistor works using conventional resistors. In the case where high power is involved, thermal issues are of significant concern which

cause the dumping load to stray from being the required $2Z_o$. This results in feedback to the Sum port and back to the transmitter, which is undesirable. The solution to this problem lays in the implementation of a Gysel modification. A Gysel power splitter is a combination of a branchline and a Wilkinson splitter. The three sections of cable connecting port 1 and 2 in Figure 5.1 are the Gysel modification. These cables take the place of the $2Z_o$ load in the Wilkison design. The benefit of this is that with the appropriate power rated cable, the cable's impedance does not vary significantly from its characteristic impedance and as such will not have the same undesirable effects as the conventional resistor used in the Wilkinson design.

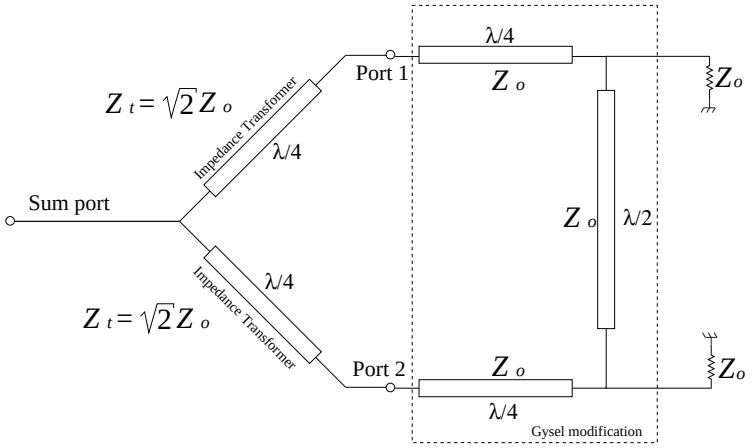

Figure 5.1: The 1:2 High-power splitter-combiner circuit with Gysel modification.

The $\frac{\lambda}{4}$ transformer section's required impedance is not equal to any of the standard impedance values available in coaxial cable, therefore the transformer sections are constructed from lumped circuit elements; i.e. inductors and capacitors. In order to determine the required characteristic impedance of the two branch lines we consider the case of the device acting as a splitter. Under normal operating conditions when functioning as a power splitter (ports 1 and 2 are terminated with 50 Ω loads), a signal enters the Sum port, it is divided between the two branches with equal amplitude and equal phase and output from ports 1 and 2. Since each end of the Gysel isolation network between ports 1 and 2 is at the same potential, no current flows through it and therefore it is decoupled from the Sum port. Each branch of the splitter in essence forms a parallel resistance. Given the requirement for 50 Ω on

the Sum port, the impedance of each branch at the Sum port needs to be $2Z_o$. The required line impedance can be calculated using the $\frac{\lambda}{4}$ transformer equation $Z_t = \sqrt{Z_i Z_l}$, where Z_i= $2Z_o$ is the impedacne at the Sum port and Z_l= Z_o is the load impedance on each of the ports . This gives us $Z_t = \sqrt{2}Z_o$.

The last stage of the design process is to calculate the values of the inductor and capacitor components to be used to create the $\frac{\lambda}{4}$ tranformer line. The inductor and capacitor values are calculated by equating their reactance at the desired frequency to the desired line impedance; in this case Z_t.

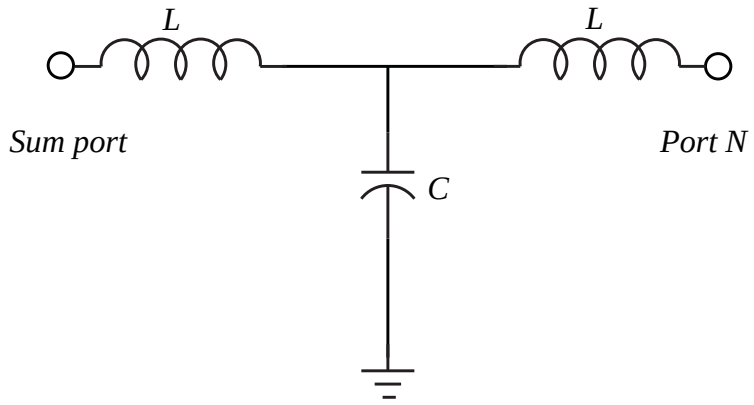

Figure 5.2: The circuit diagram of a lumped element quarter wave transformer circuit. Coaxial cable is only available with a specific set of standardised impedances. Since the required transforming impedance does not correspond to one of these standardised impedances, the transmission line needs to be fabricated out of lumped circuit elements in order to achieve the required transforming impedance for the quarter-wave transmission line.

The values for inductance and capacitance are calculated using the following two equations.

$$\omega L = Z_t = \sqrt{2}Z_o \tag{5.1}$$

$$\frac{1}{\omega C} = Z_t = \sqrt{2}Z_o \tag{5.2}$$

Using 5.1 and 5.2, $\omega = 2\pi f$, $Z_o = 50\Omega$ and f= 55MHz we get:

$$L = \frac{50\sqrt{2}}{2\pi f} = 0.0205\ \mu\text{H} \tag{5.3}$$

$$C = \frac{1}{2\pi f 50\sqrt{2}} = 40.9 \text{ pF} \tag{5.4}$$

These values are not the final values for the components as there is some tuning involved due to stray capacitance and inductance between neighbouring components, metallic devices and the mounting PCB. The final step is to calculate the length of the cables required for the Gysel section as they need to be cut to the appropriate electrical length taking into account that LMR-600 cable has a velocity factor v_f= 0.86 and the free-space wavelength at f= 55MHz is λ= 5.45m. The cables are cut as follows:

$$L_{\frac{\lambda}{2}} = \frac{v_f \lambda}{2} = \frac{0.86 \times 5.45}{2} \approx 2.34 \text{ m} \tag{5.5}$$

$$L_{\frac{\lambda}{4}} = \frac{v_f \lambda}{4} = \frac{0.86 \times 5.45}{4} \approx 1.17 \text{ m} \tag{5.6}$$

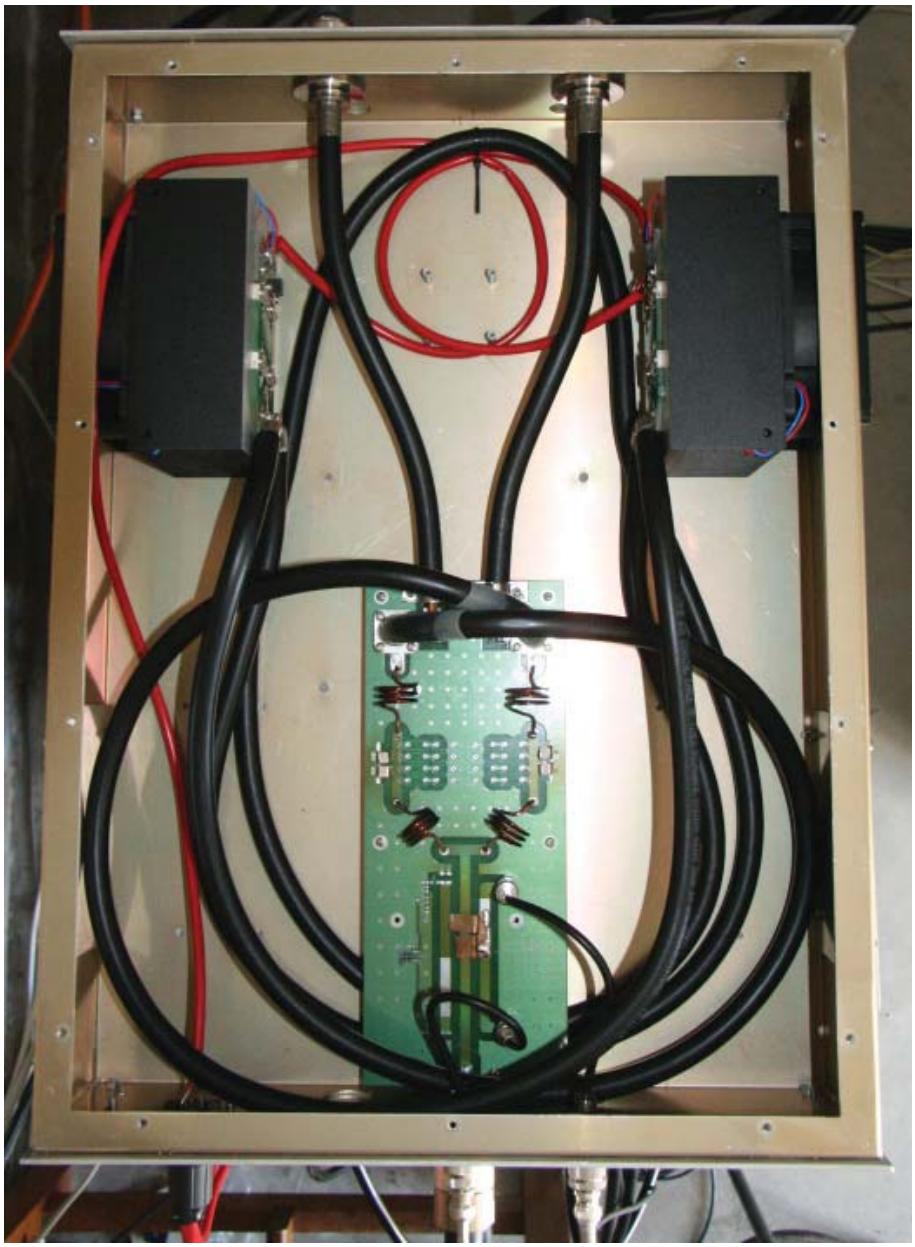

Figure 5.3: The 1:2 Gen-1 splitter-combiner finished product. The two square black heat sinks in the top two corners of the box are 50 Ω dummy loads. These are used in the event of mismatch at one of the ports on the splitter-combiner. The two short runs of cable forming a "Y" are the two output ports of the the splitter which, connect the actual splitter circuit to the output panel of the box. The curl of black cables is the Gysel modification circuit. The square copper tabs over the Sum track on the PCB are part of an RF directional coupler. There are used to sense the Sum port line current such that voltage measurements can be made on the forward and reverse monitor ports. The red cable is a 24 V DC power line for providing power to the fans on the heat sinks which are used for cooling purposes.

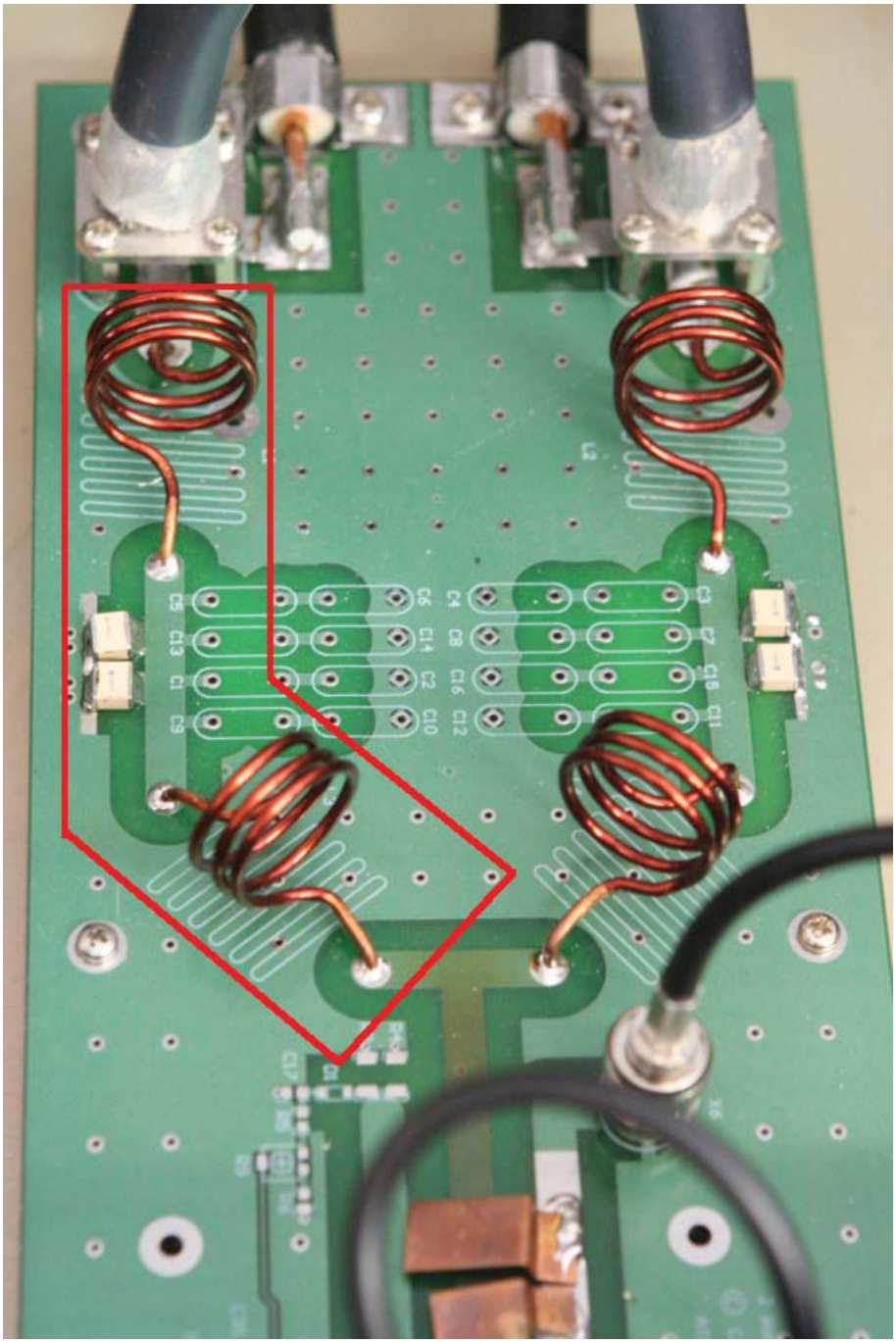

Figure 5.4: the Gen-1 PCB board which contains the 1:2 splitter-combiner circuit. The circuit path contained within the red box is the $\lambda/4$ transmission line which performs the necessary impedance transformation between the Sum port and port 1.

After the accidental failure of the LMR-900 feeder cable which led to the destruction of the Gen-1 splitter-combiner, a replacement combiner was constructed to be used with the new STX-II transmitter system. The new splitter-combiner is no longer required for meteor operations, but is integral to the operation of the radar in ST mode. The main differences between the first and second generation splitter-combiners is in the monitoring of temperature and power inside the box and the refinement of the box's tuning capability. Gen-1 only utilised the direct measurement directional coupler as well as an internal temperature sensor on each dummy load to activate the fans once the the temperature inside the box rose above 50°C. The new splitter-combiner has this capability, but also utilises hardware to remotely monitor the power and temperature inside the box (see Figures 5.6 and 5.8). In order to improve the tuning of the splitter-combiner, extra capacitance was introduced into the $\lambda/4$ transformer sections with a tunable inductor in parallel (blue boxes Figure 5.6) such that it could be tuned accurately to a return loss $\Gamma \sim$ -50 dB at 55 MHz (see Figure 5.7). This was an improvement over the Gen-1 tuning which was $\Gamma \sim$ -35 dB at 54.1 MHz.

5.2 Summary

The goal was to design and construct a 1:2 splitter-combiner that would be capable of handling the large amount of power required at 55 MHz in order to feed the high-powered crossed-dipole transmit antenna. The splitter-combiner itself went through two stages of evolution, the first generation was used to split the 6 combined outputs from the VTX transmitter in order to feed the transmit antenna. While the first design proved to be satisfactorily tuned at 55 MHz, the accidental failure of the LMR-900 feed cable on the sum-port lead to irreparable damage to the splitter-combiner. At the same time, the VTX transmitter was replaced by a new 40 kW STX-II transmitter which had two outputs that could feed the meteor transmit antenna directly. The second generation splitter-combiner would subsequently be used for Sratospheric-Tropospheric (ST) operations. The STX-II transmitter has two outputs for meteor operation and two outputs for ST operations. The two ST outputs could be combined into one and subsequently split into the required six channels; in essence the reverse of the VTX configuration. The second generation also contained a few refinements for better centre frequency tuning and return loss as well as hardware for monitoring the power

flowing through the splitter-combiner remotely. In the next chapter we investigate the radar system output power characteristics as well as verify the meteor echo rate formula published by McKinley [1961] using the developed high-powered antenna and splitter-combiner hardware.

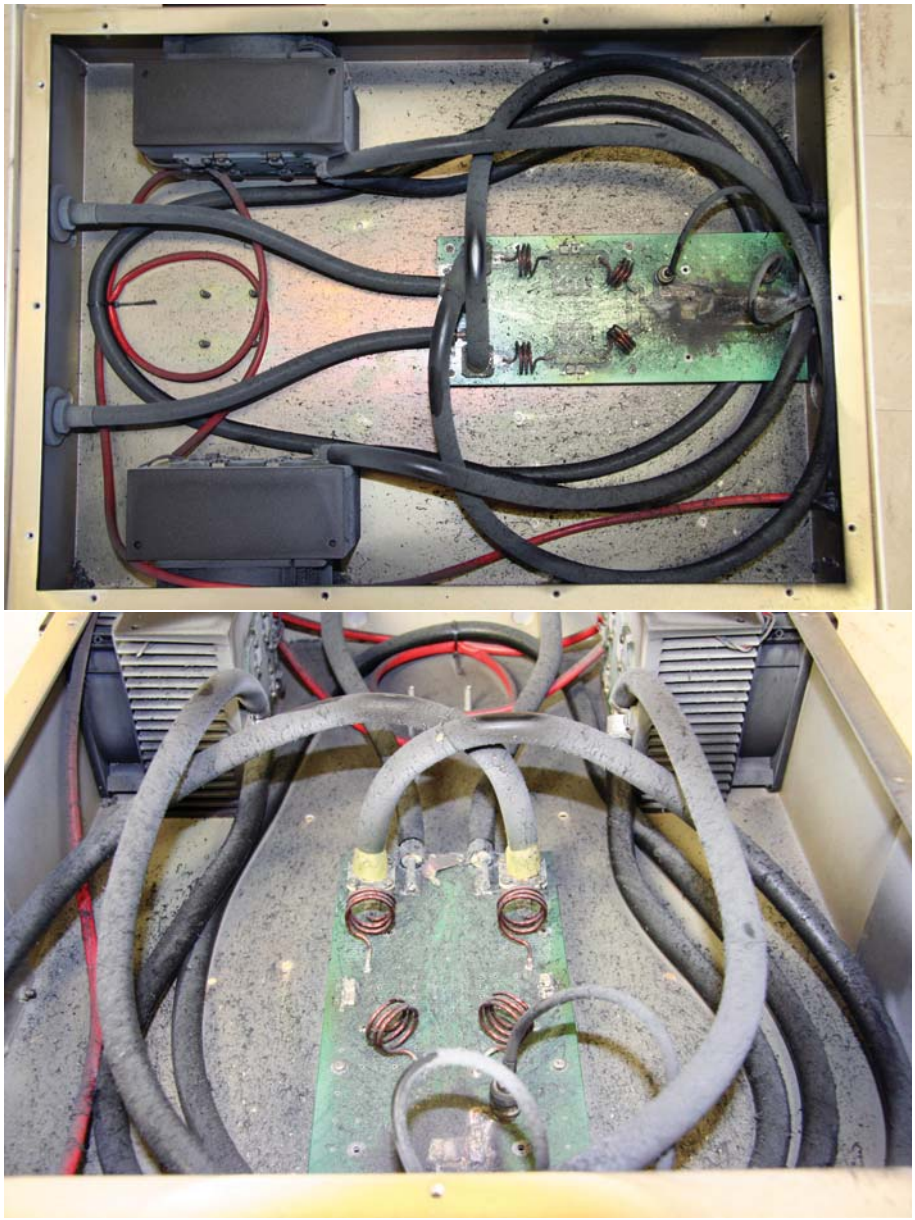

Figure 5.5: The remains of the first generation 1:2 splitter-combiner after the failure of the LMR-900 feeder cable. Photograph by Daniel McIntosh.

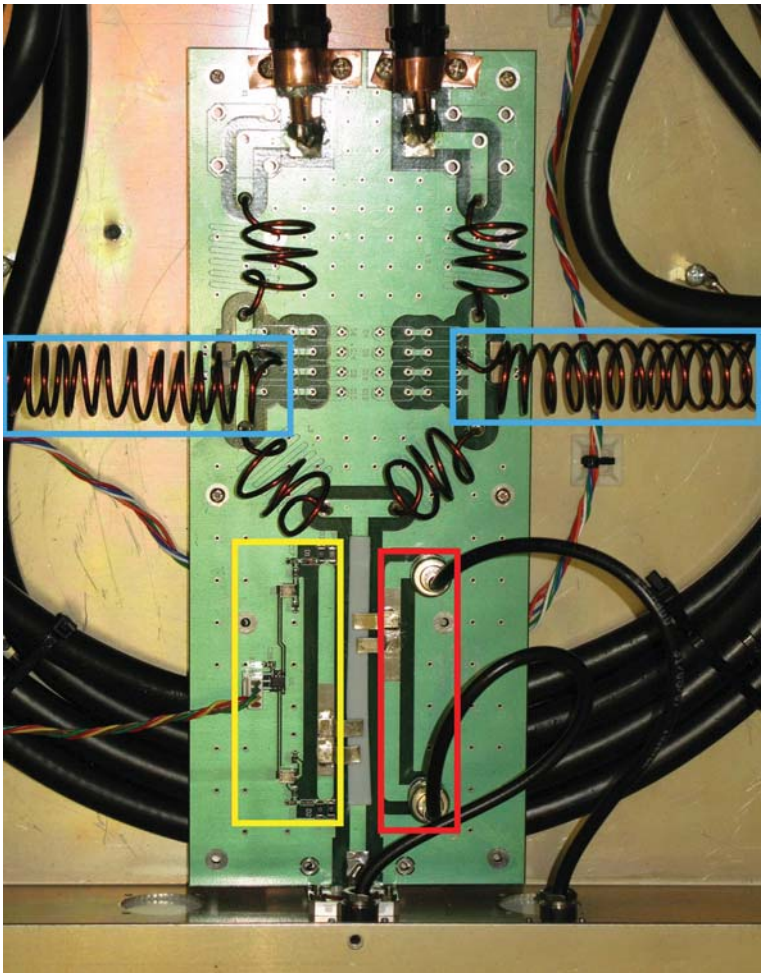

Figure 5.6: The Gen-2 1:2 splitter-combiner. The red and yellow boxes contain the directional power couplers which are used to estimate the power flowing through the Sum port. The coupler in the red box is connected to monitor ports on the face panel of the box for direct measurement. The coupler in the yellow box interfaces with some digital logic such that the power can be monitored via the STX-II's remote monitoring software. Photograph by Daniel McIntosh.

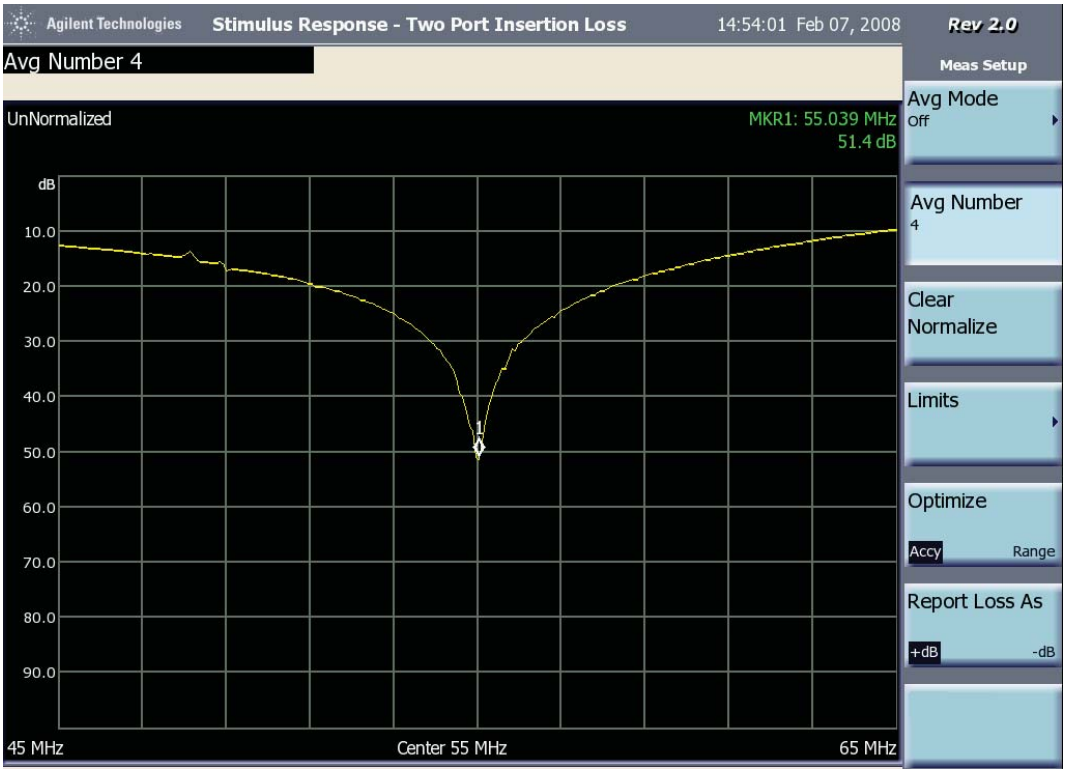

Figure 5.7: The 1:2 splitter-combiner insertion loss measurement. The first generation splitter-combiner achieved a return loss of 35 dB down. With the addition of the extra tuning inductors as can be seen in Figure 5.6 an insertion loss close to -50 dB down was achieved.

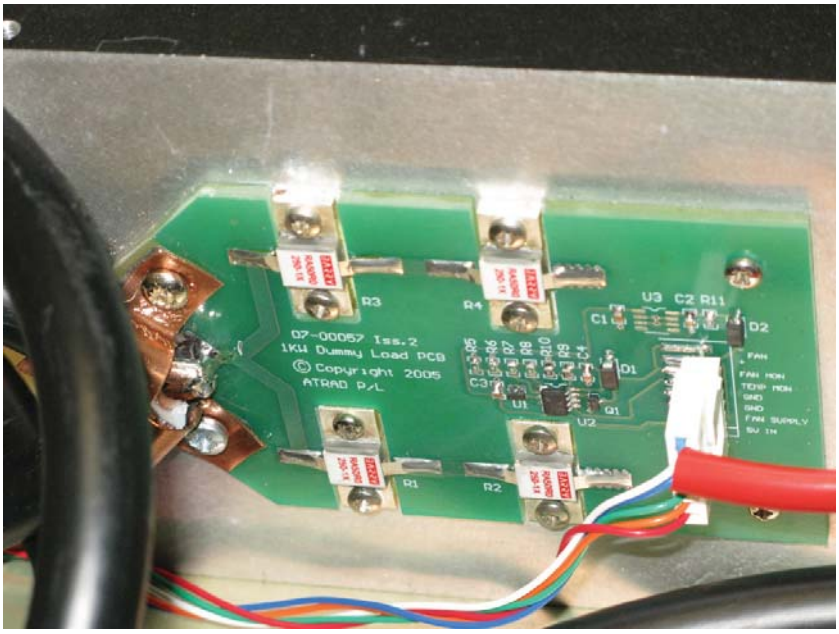

Figure 5.8: Gen-2 dummy load.

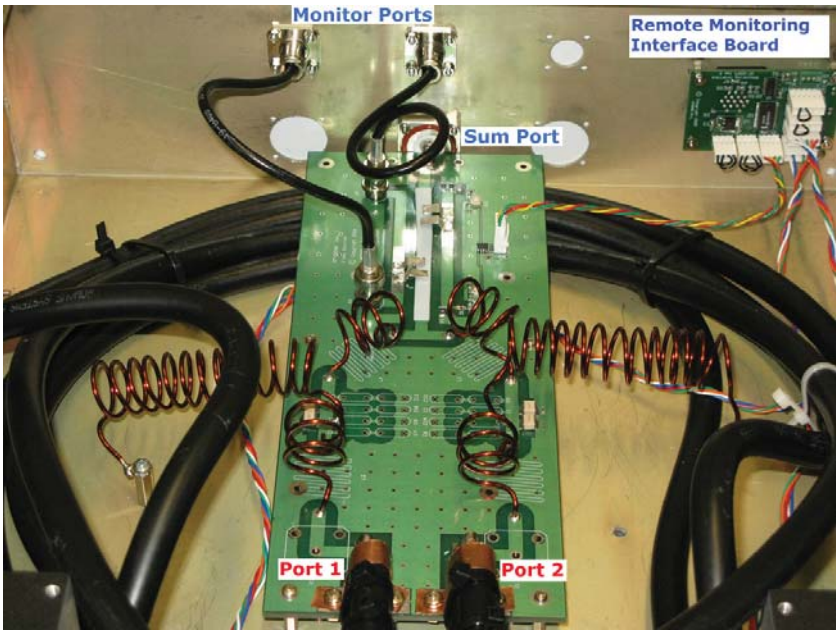

Figure 5.9: The 1:2 splitter board with remote monitoring interface board.

Chapter 6

Meteor Echo Rate Observations

6.1 Verification of McKinley Daily Echo Rate Formula

In 1961 McKinley published a book entitled "Meteor Science and Engineering" which (6.1) provides a quantitative means of relating typical radar parameters to the observed hourly echo rate. For a particular meteor system the echo rate is given by

$$N \propto \frac{P_t^{1/2} G \lambda^{3/2}}{P_r^{1/2}}, \tag{6.1}$$

where P_t is the radar transmit power, G is the product of the gain of the radar transmit and receive antennas (i.e. $G = G_t^{1/2} G_r^{1/2}$), λ is the carrier wavelength of the radar transmit signal and P_r is the received echo power from a meteor echo. The justification of this formula can be found in the paper entitled "Variation of meteor echo rates with radar system paramters"[McKinley, 1951]. What is not emphasised in McKinley's book is that the power terms in (6.1) refer to the average transmit and receive power. The key point of (6.1) is that the echo rate fundamentally depends on the radar wavelength or frequency. At a first glance it would seem that by simply lowering the frequency (increasing the wavelength) to a substantially low frequency (e.g. 2 MHz), this would dramatically increase the observed echo rate. This would be true, however partial reflections of the signal from the ionosphere become a factor due to layers of electrons in the ionosphere induced by solar radiation during the day time [Gardner and Pawsey, 1953, Belrose, 1970, Cervera et al.,

2004]. In actual fact it was the use of MF radar that lead to the discovery of meteor ionization trails as a source of reflection for MF radar during the much quieter night time periods where the E-region undergoes depletion [McKinley, 1961].

We seek to further clarify (6.1) such that we may have a clearer means of establishing a meteor radar system's performance at any one particular time. As such, an experimental procedure was devised in order to verify the relationship between a particular radar system's characteristics and the observed daily echo rate. The experimental procedure involved operating BP VTX and STXII systems at various power levels in an experimental sequence over the course of several days and then averaging and weighting the results accordingly. Initially, an experimental sequence was chosen such that the radar would run a repetitive 8 minute sequence (2 minutes per experiment) where the output power would increase by 25% each time, from 25% to 100%, and then repeat. This would provide an effective observation duty cycle of 25% for each power level and as such the daily echo rate for each power setting would need to be multiplied by 4 to obtain the equivalent of running the radar at that power level for an entire day. A 25% power increment proved to be too coarse a result and a 10% increment was chosen to provide a better result. Although the maximum peak output power for each system was known, this needed to be verified along with the output power of the radar systems at each power level setting. The power level percentage setting was made within the radar configuration software. As it turns out, the relationship between the setting in the radar configuration software and the true peak output power of the radar was in fact non-linear, as can be seen in Figures 6.1, 6.2, and 6.3. As such this non-linearity needed to be established and accounted for when verifying 6.1.

6.1.1 Establishing Radar Output Power Curves

When determining calibration factors for measurement instrumentation it is important to account for all possible points of loss associated with instruments and cables. A single cable loss of up to 0.5 dB can result in the final measurement containing a significant error associated with it and hence not represent the true value. The VTX meteor system output power that was being fed to the Tx antenna was measured via the forward monitor port on the 1:2 splitter. This required knowing the associated calibration factor for

that port. The method for determining the associated calibration factor is outlined in Appendix B. The procedure assumes that when performing the measurements, all associated losses with cables and hardware transmission paths are known and can be accounted for when calculating the actual true voltages and powers on the output ports. With the STX-II system the 1:2 splitter-combiner is reversed and used for ST operations. It is possible to use the monitor ports on the 1:2 to estimate the output power for the radar system; however it will not give a true indication of the power being fed to the meteor Tx antenna as there is loss associated with the splitter-combiner and the parameters used for ST experiments differ greatly from that of meteor experiments. The optimum means of measuring the output power to the Tx antenna is to measure directly on the output of the 12:2 combiner as this is fed directly to the Tx antenna via a switching relay, which is considered to have negligible loss.

VTX Power Curve

Figure 6.1 shows the results of measuring the output power from the 1:2 splitter-combiner box which fed the meteor transmit antenna. The black line (14/9/2007) shows the output power relation with respect to the power setting in the radar configuration suite prior to any tuning of the individual PA modules of the VTX transmitter. The blue curve (5/10/2007) represents the result after an initial tuning attempt. The green curve (20/20/2007) represents the final tuning of each of the PA modules after replacing several of the capacitors in each PA on the cathode of the valves as well as replacing some of the capacitors in the RF-drive modules of each of the PAs. The orange curve illustrates the importance of factoring in all possible sources of loss, and represents the 20/10/07 result obtained prior to having factored in the losses associated with the LMR-195 phase matched cables which were used to connect the oscilloscope to the the monitor port of the 1:2 splitter-combiner. Tuning of each of the PA modules involved terminating PA 1 and 2 with dummy loads and using two 40 dB sniffers to measure the output signal from the PA. PA 1 was selected to be in the initial reference signal to which all other PAs would be matched to. Tuning of the individual PAs involved adjusting variable capacitors to adjust the amplitude and phase of the output signal. Once the maximum amplitude signal was obtained from PA 1 without distorting the pulse shape, PA 2's variable capacitors were adjusted such

that the output signal was comparable in amplitude and phase with PA 1; most importantly in phase. This process was repeated for the remaining PA modules. Phase coherence was considered the most important aspect as each of the signals from the six PA modules were combined via a 6:1 combiner and then split via the 1:2 splitter. In order to achieve maximum output power, phase coherence between each transmitter module was essential.

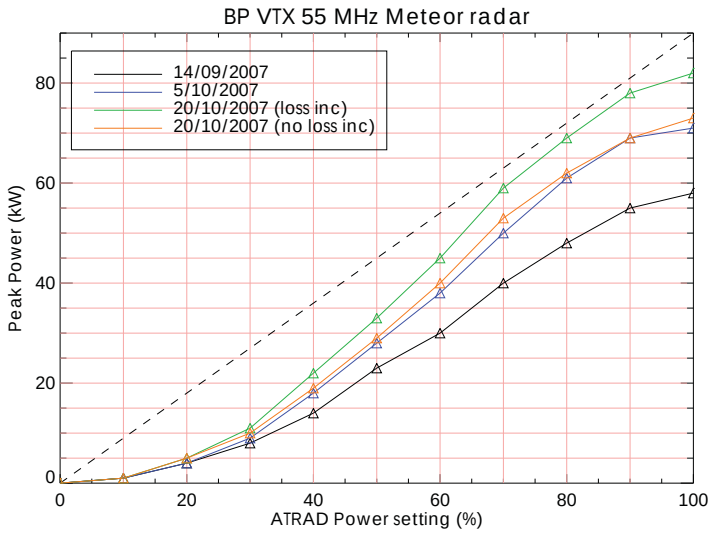

Figure 6.1: VTX calibration results. The black curve represents the results from the initial measurements prior to tuning the PA modules of the VTX. The blue curve represents the results after an initial tuning. The green (losses included) and orange (losses not included) curves represent the results from the final tuning. The orange curve is included for completeness and to demonstrate the importance of accounting for all potential sources of loss which may affect measurements of signal amplitude. The dashed line represents an ideal linear relationship with the maximum output power at 100% corresponding to the manufacturer's marketed full output power for the system.

STX-II Power Curve

Figure 6.2 shows the results of measuring the output power from the STX-II transmitter which replaced the VTX transmitter. Initially it was thought that due to the higher duty cycle of the transmitter (10% as opposed to the VTX's 4%) that a direct measurement of the output power from the transmitter would not be possible. As such, this would have meant measuring the power on the monitor port of the rebuilt 2:1 combiner. This was not the most ideal situation as the 2:1 combiner was to be used for ST experiments and not for meteor experiments, which meant running the radar with non-meteor parameters as well as having another source of un-factored loss in the measurements. The green curve represents the results from the measurements made prior to accounting for all sources of loss and the blue curve represents the results from the same set of measurements with all identified sources of loss accounted for in the calculations. The measurements on the outputs of the 12:2 combiner were made possible by establishing a sequence of very short, low duty cycle experiments such that the average power would be low enough in order to place dummy loads on the outputs along with a pair of 40 dB sniffers. The peak power would remain the same between the modified low duty cycle experimental sequence and the actual sequence to be run which means that running the modified sequence would have no bearing on determining the calibration curve and the verification of (6.1). The black curve represents the measurements made on the outputs of the 12:2 combiner (essentially the output of the transmitter) with all identified sources of loss factored in.

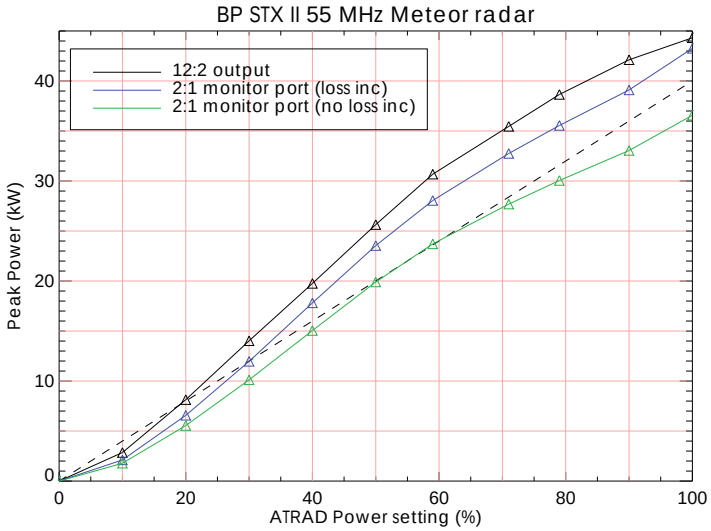

Figure 6.2: STX-II calibration results. The black and blue curves represent measurements of the transmitter output power at different points in the system. The green curve represents the results from measurements on the 2:1 combiner without accounting for cable losses. The dashed line represents an ideal linear relationship with the maximum output power at 100% corresponding to the manufacturer's marketed full output power for the system.

STX I Power Curve

Figure 6.3 shows the results of measuring the output power from the STX I transmitter used for the Darwin meteor radar system. The three solid state PA modules are combiner into two outputs via a 3:2 combiner. Since the system has a lower peak output power, and as such lower average power, direct measurement on the outputs of the combiner were made in order to determine the output power from the transmitter. In this case the transmit antenna was tuned accurately to 50 $\pm 0.1j\Omega$. The blue curve represents the measured output power from the radar.

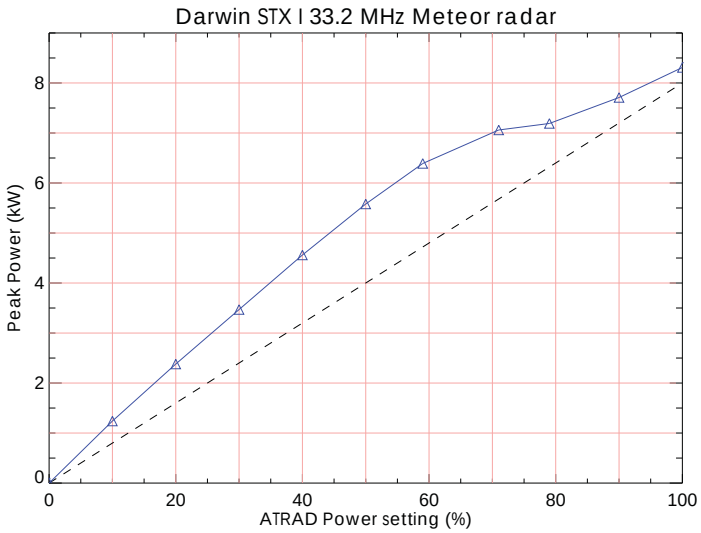

Figure 6.3: STX I calibration results. The dashed line represents an ideal linear relationship with the maximum output power at 100% corresponding to the manufacturers marketed full output power for the system.

6.2 Receiver Gain Calibration

We can use (6.1) along with the experimental results of the daily echo rate measurements as a function of transmit power to estimate the received echo power term P_r in (6.1). The radar transceiver produces I and Q signals which together with the 16-bit data acquisition card would represent a ±10 V range on I and Q ports as ±32767 A-to-D counts in the ATRAD time series analysis suite viewer. For a detailed description of the A-to-D process see Chapter 3. The receiver calibration was determined by feeding in a reference signal of suitable amplitude to the receiver front end slightly off centre frequency such that the signal would appear as a Doppler shifted signal and be present after the down mixing to base band process. For this a frequency of 55.00056 MHz was used. The calibration was set up as can be seen in Figure 6.4. The CRO was used to ensure that the signal input was not being clipped by the time it reached the final output stage of the transceiver and the receiver was not being saturated. The RF output from the signal generator was set to to -100 dBm[1] (=2.236 μV_{rms}). A signal of amplitude 4 V_{pp} was then measured on the I port. In A-to-D units this is

[1]0 dBm corresponds to 1 mW into $50\Omega \equiv 0.2236 V_{rms}$

$$\frac{4/2}{10} \times 32767 = 6553.$$

This also corresponds to a voltage gain from the receiver front end to acquisition card

$$G_v = 20 \log_{10} \left(\frac{4}{6.32 \times 10^{-6}} \right) \simeq 116 \text{ dB}. \tag{6.2}$$

Using this information we can then take the amplitude of a typical meteor echo and work out what voltage this corresponds to on the receiver front end. We then account for cable loss and antenna gain characteristics to arrive at an approximate value for the signal voltage measured on the antenna. Given this voltage goes into a 50 Ω load we can work out what the power from a received echo is.

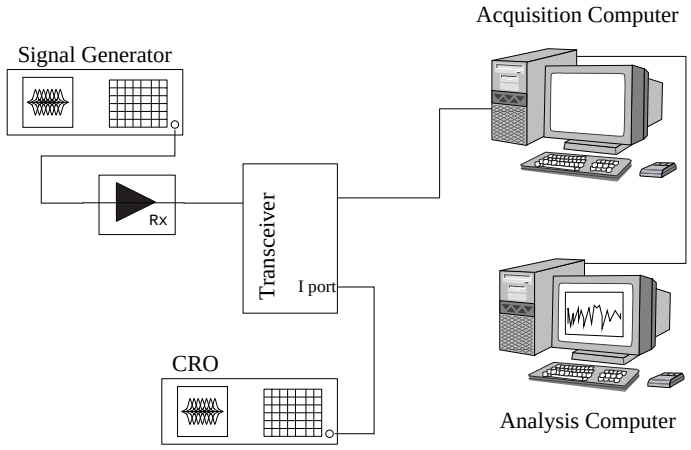

Figure 6.4: Receiver calibration measurement setup as performed on the BP meteor system.

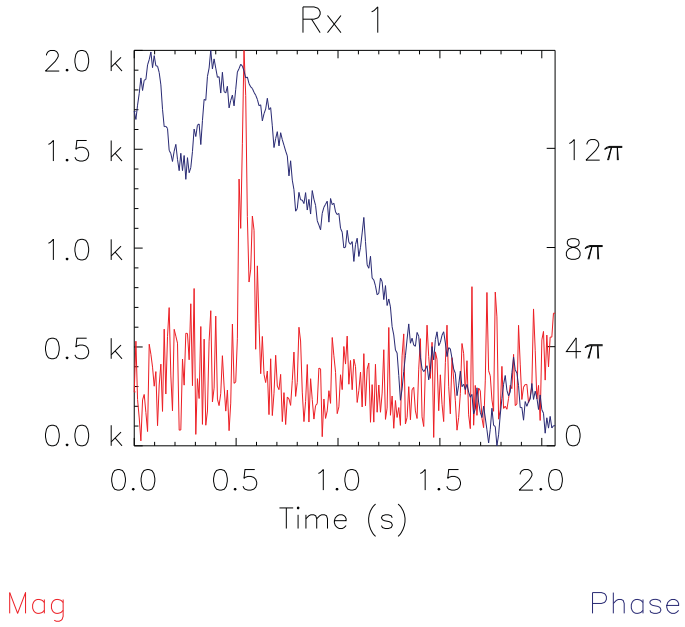

Figure 6.5: An example of a underdense meteor echo detected by the BP 55 MHz meteor radar system. The red line is the echo magnitude and the blue line is the phase measured. The left Y-axis is the amplitude in A-to-D units and the right Y-axis is the phase in radians.

Cervera and Elford [2004] quote a result for the minimum electron line density based upon radar system parameters and received echo power. The expression for the minimum line density is as follows

$$q_{\min} = 6.3 \times 10^{15} \left(\frac{R}{\lambda}\right)^{3/2} \left(\frac{P_r}{P_t G_t G_r}\right)^{1/2} (\alpha_r \alpha_v \alpha_d), \tag{6.3}$$

$$\alpha_r = \exp\left(\frac{-4\pi r_0^2}{\lambda^2}\right), \tag{6.4}$$

$$\log_{10} r_0 = 0.0194h - 1.96 + 0.6 \log_{10}\left(\frac{v}{40}\right), \tag{6.5}$$

$$\alpha_v = \frac{1 - e^{\Delta}}{\Delta}, \tag{6.6}$$

$$\Delta = \frac{16\pi^2 D}{v} \left(\frac{R}{2\lambda^3}\right)^{1/2}, \tag{6.7}$$

$$\alpha_d = \frac{\tau}{T e^{(N-1)T/\tau}} (1 - e^{T/\tau}), \tag{6.8}$$

$$\tau = \frac{\lambda^2}{16\pi^2 D}, \tag{6.9}$$

viz.

$$P_r = \left(\frac{q \alpha_r \alpha_v \alpha_d}{6.3 \times 10^{15}}\right)^2 \left(\frac{\lambda}{R}\right)^3 P_t G_t G_r. \tag{6.10}$$

Underdense line charge densities range from $1\times10^9 - 1\times10^{14}$ m^{-1} [McKinley, 1961, Cervera and Elford, 2004] with the transition between underdense and overdense occurring between $10^{13} - 10^{15}$ m^{-1}. As can be seen from the expressions above, the received echo power is dependent upon many factors, not the least of which is the echo's location and physical characteristics. In order to obtain an initial value for received echo power we have selected a model echo with the parameters listed in Table 6.2.

Equation parameters	
R	Range to the echo (m)
λ	Radar wavelength (m)
P_r	Received echo power (W)
P_t	Average transmit power (W)
G_t	Transmit antenna gain
G_r	Receive antenna gain
α_r	Reduction in amplitude due to finite initial radius of the meteor trail
α_v	Echo amplitude attenuation due to the finite velocity of the meteoroid
α_d	Meteor echo selection effect
r_0	Initial trail radius (m)
h	The height of the echo (m)
v	Velocity of the meteoroid km.s^{-1}
τ	Decay time of the echo (s)
T	Inter pulse period (s)
D	Ambipolar diffusion coefficient m^2.s^{-1}
N	Detection criterion of N pulses above limiting signal level

Table 6.1: Parameter description list for the above equations. Definitions for the parameters can be found in McKinley [1961], Peregudov [1958], Baggley and Webb [1980], Cervera and Elford [2004]

Underdense meteor echo model	
Parameter	characteristic
height (h)	90 km
AOA (Zenith)	45°
D	3. m^2.s^{-1}
v	40 km.s^{-1}
q	1×10^{13} m^{-1}

Table 6.2: Meteor underdense echo parameters. The values for v and q are arbitrary. The values for zenith AOA and height were selected as examples of where the majority of echo detections occur.

Using the model parameters along with the radar parameters listed in Table 3.2 it was found that the receive echo power measured by the VTX was calculated to be 4.75×10^{-15} W and for the STX-II 6.19×10^{-15} W. These values were obtained by investigating the raw data files to find meteor echoes with typical underdense characteristics as can be seen in Figure 6.5. It was found that underdense echo amplitudes ($V_{\text{A-to-D}}$) were found to range from 1500 to 2500 A-to-D units. As such the corresponding voltage on the front end of the receiver was calculated using the receiver gain that was calculated above along with

$$\frac{V_{\text{A-to-D}}}{6553}\frac{2V_{\text{pp}}}{2\sqrt{2}} = V_{rms} \tag{6.11}$$

This voltage was then converted to the voltage as seen on the receiver front end using the gain calculated in (6.2). For simplicity it was assumed that the antenna gain was countered by the cable loss and as such the effect of combination of these factors was assumed to be negligible on the measured voltage; i.e. the receiver front end voltage corresponds to the signal amplitude voltage from the return echo. Table 6.3 below contains calculated power values based upon measured echo amplitudes and the measured receiver gain.

Underdense meteor echo power		
$V_{\text{A-to-D}}$	V_{rms} $\text{Rx}_{\text{F/E}}$	Power (W)
1500	2.57×10^{-7}	1.32×10^{-15}
2000	3.42×10^{-7}	2.34×10^{-15}
2500	5.60×10^{-7}	6.28×10^{-15}

Table 6.3: Meteor echo powers measured on the BP VTX system.

These results will be used in the verification of (6.1) and can also be used along with the meteor range and angle of arrival information to determine electron line densities for detected trails. If we use the model parameters in table 6.2 and calculate the theoretical received echo powers as a function of line charge density using (6.10), then we obtain the curves in Figure 6.6

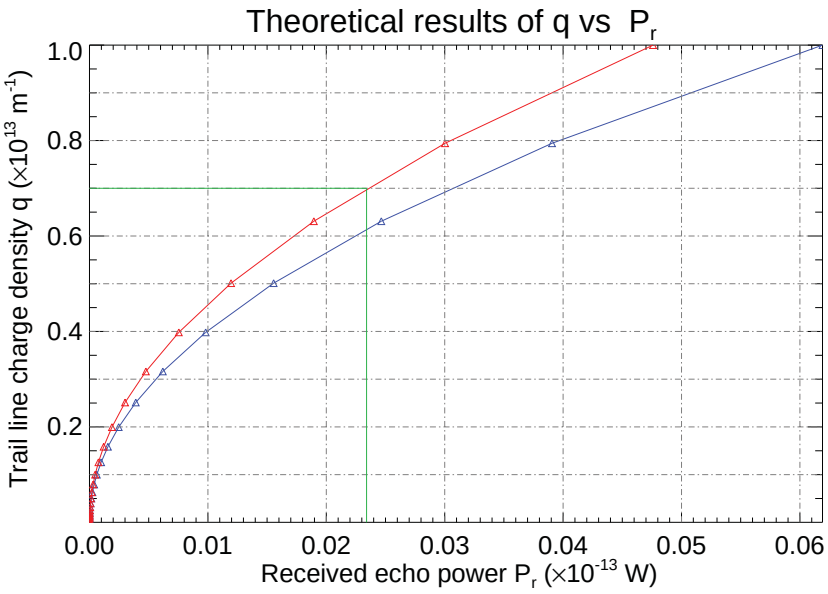

Figure 6.6: The red curve is the result using the model and VTX experiment parameters and the blue curve is the result using the model and STX-II experiment parameters. From these curves we can derive the line charge density from a particular measured echo power. The green lines indicate the echo power measurement obtained from the VTX 55 MHz BP system and the corresponding value $q = 7 \times 10^{-12}$ m^{-1}.

6.2.1 Meteor Echo Rate Observations as a Function of Power and Wavelength

This experiment involved operating the Buckland Park and Darwin radar systems in a manner similar to what was established in section 6.1.1 whereby an experimental sequence was set up, which varied the transmit power from 10% to 100% in 10% increments. This sequence was operated over the course of several days with the analysis computer analysing the raw data files created for each power experiment and producing an associated *".met"* file for each power experiment. The .met files are analysed data files produced by the analysis PC which contain information about individual echo detections such as time of detection, AOA, echo decay time, diffusion coefficient, radial component of wind velocity, Signal-to-Noise ratio (SNR), etc. As there were 10 power settings, this equated to an observation duty cycle of 10% and the resultant daily echo rate was multiplied by 10 to obtain the equivalent of operating the radar for a full day at that power level. The total daily echo results for the period of observation were averaged to provide a single daily echo rate. The results for the BP experiment can be seen in Figure 6.7. We can see from the plot that the daily echo rate does indeed increase as the square-root of the transmitted power. The VTX transmitter has a greater peak power than the STX-II, however it has less average power on account of the duty cycle of the experiment. What is made clear is that the relationship in (6.1) does in fact show the dependence on the average power of the system as opposed to the peak transmit power of the system as the STX-II is able to obtain higher daily echo rates. Despite this expression in (6.1) being for the hourly count rate, we may still use this as an indication of a particular meteor radar system's performance without requiring a detailed knowledge of the meteor response function which describes expected echo rates at different heights and times based upon radiant distributions and the Earth's motion [Cervera and Elford, 2004, Cervera et al., 2004]. The meteor response function also serves to explain the observed seasonal variation in echo rates as a function of a particular systems geographical location.

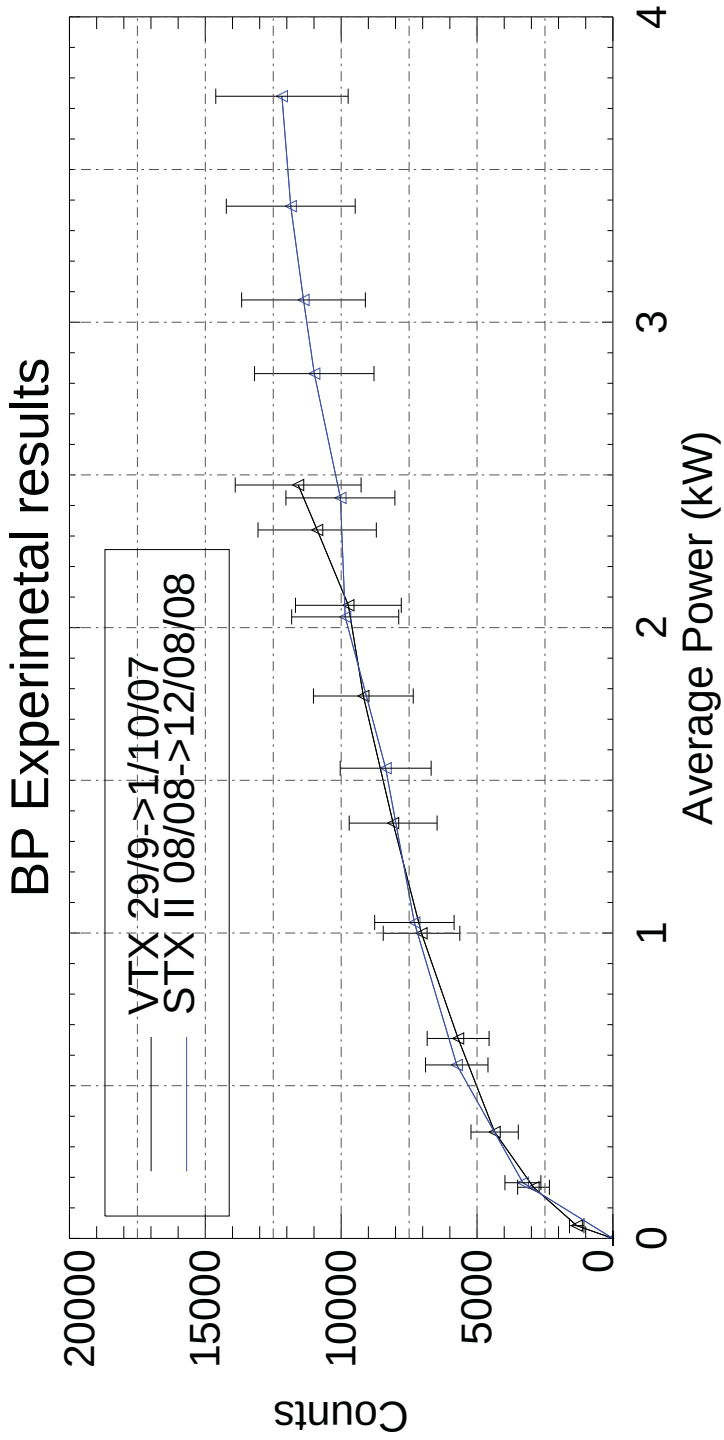

Figure 6.7: Experimental results for BP echo rate experiment.

We can re-write (6.1) to relate to the echo rate for a 24 hour period as follows

$$N = \beta \left(\frac{P_t}{P_r} \right)^{1/2} G_t^{1/2}(\theta, \phi) G_r^{1/2}(\theta, \phi) \lambda^{3/2}, \tag{6.12}$$

where P_t is the transmitted power, P_r is the received power, $G_t(\theta, \phi)$ and $G_r(\theta, \phi)$ are the transmit and receive antenna gain respectively as a function of azimuth and zenith angle and λ is the radar wavelength. It should be noted that the transmit and receive antennas used for the all-sky systems in this study have relatively constant gain over the azimuth and zenith angles where the majority of meteor echoes are detected. As such we may take $G_t(\theta, \phi) = G_r(\theta, \phi) = G$. We have all the information we need in order to determine a value for β, where β is our proportionality factor to be determined. In (6.12) we have expanded to a more general form which illustrates the dependance upon antenna gain as a function of both the azimuth and zenith angles. For the BP and Darwin systems, which use crossed dipole antennas, we can assume that the gain is relatively constant over the range of azimuth and zenith angles where the majority of meteors are detected from. For the value of P_r we use the minimum detectable power level for the receivers based upon the experiment configuration. We can calculate this as follows

$$P_r = kT_r \Delta f, \tag{6.13}$$

where k is Boltzman's constant ($k = 1.38 \times 10^{-23}$ W.s.K^{-1}), T_r is the system temperature (K) and Δf is the receiver bandwidth (Hz) used. ATRAD provide a 3 dB Noise Figure (NF) for their receivers which we can use to calculate the Noise Factor (F) and subsequently T_r as follows

$$\begin{aligned} F &= 10^{NF/10} && (6.14) \\ &= 1.995 \\ T_r &= (F-1)T && (6.15) \\ &\approx T \\ &\approx 300K. \end{aligned}$$

Using the BP VTX based experiment bandwidth ($\Delta f = 18.1$ kHz) we estimate the minimum detectable power level to be $P_r = 7.5 \times 10^{-17}$ W. For an STX-II based experiment ($\Delta f = 36.6$ kHz) $P_r = 1.5 \times 10^{-16}$ W. We have calculated a range of β values based upon the variation of echo rate and

transmit power observations depicted in Figure 6.7. It is important to note that β in itself is not a true constant as it will vary based upon the time of year and implicitly has units of $m^{-3/2}$, but it will however allow us to gain insight for a system's performance for this particular time of year when the observations were made. We can see the results of the calculation of the β value for both the VTX and STX-II systems in Figure 6.8. Using the derived β values for both the VTX and STX-II, the theoretical count curve was calculated and plotted in Figure 6.9. In order to further refine β we need to perform the count rate experiment for each month of the year in order to determine how β varies through the year and also at different geographical locations in order to determine its variation with latitude. We have however moved a step closer to refining the expression given by (6.1) in order to characterise a particular meteor radar systems performance based upon the manufacturer's specifications and experimental setup. Due to technical difficulties with the Darwin meteor radar, no results were obtained for that system.

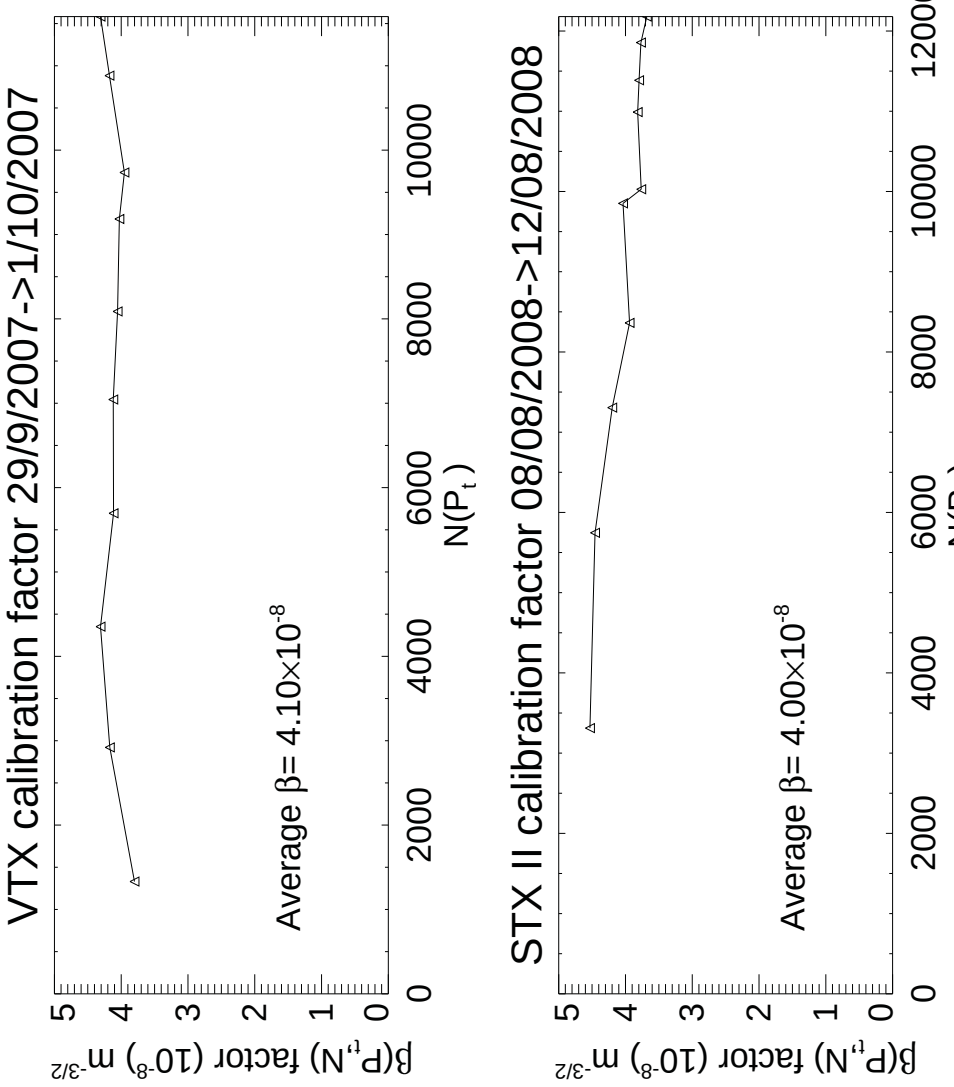

Figure 6.8: Echo rate calibration factor. Both of these plots show the calibration factor determined at a frequency of 55 MHz.

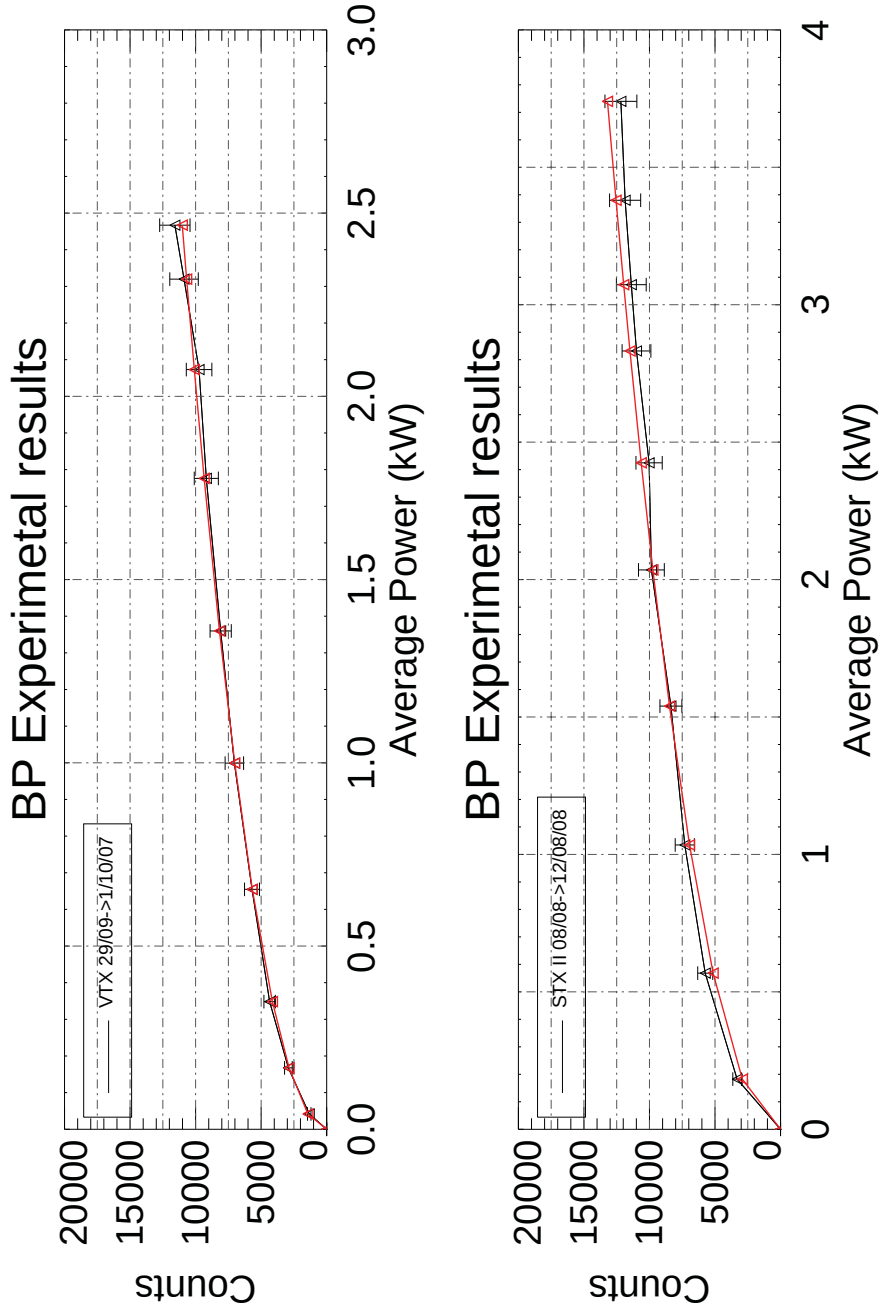

Figure 6.9: The black lines correspond to the experimental results obtained and the red lines correspond to the theoretically derived result using the established β factor. The VTX result has a correlation of 0.998 and the STX-II has a correlation of 0.996.

6.3 Summary

In this chapter the echo rate formula published in McKinley [1961] was verified against experimental results along with the establishment of the radar power calibration curves and method for determining the calibration factor for the receiver system from receiver front-end to raw data acquisition display. Establishment of the receiver gain factor was a critical step in determining the received echo power from a 'typical' underdense meteor echo that could then be used in the verification of (6.1). It was found that the radar output power response to the variation of power setting in the radar configuration was very much non-linear. This was a critical result when performing the count rate experiment which involved varying the power percentage setting in the radar configuration as it allowed for an accurate match up between average observed echo rates and the corresponding transmit power setting. Equation (6.1) represents the hourly echo rate and as such a proportionality factor (β) needed to be determined to relate it to the daily observed results. The value for β was consistent over the two observation periods which occurred at similar times of the year for two different years. An average value of $\beta \sim 4\times10^{-8}$ was obtained, however further experimentation at other times of the year and comparison with existing work on the meteor response function [Cervera et al., 2004, Cervera and Elford, 2004] is required to determine a relation for β that is applicable throughout the course of the year. The use of the β factor in (6.12) resulted in strong agreement observed between the theoretically calculated echo rates and the experimentally measured echo rates in Figure 6.9. While the argument appears somewhat recursive and use of the meteor response function should be taken into account, the experimental results show the terms in (6.1) determine the shape of the count curves and hold true.

One of the issues associated with the meteor technique when determining atmospheric parameters is the lack of echoes (statistical samples) in certain range-time bins. Equation (6.1) tells us that in order to improve the echo rate, we need to vary either the frequency of observation or the amount of transmitted power. Given the restrictions of frequency allocation in Australia, the verification of (6.1) means having to increase output power in order to increase the echo rate. This result also validates the development of the BP hybrid system as discussed in the previous chapters. Now we make use of the increased echo rate to determine the statistical reliability of atmo-

spheric parameters derived using the meteor technique. This is discussed in the following chapters.